Title: Signal transduction pathways controlling *Ins2* gene activity and β cell state transitions

Authors: Chieh Min Jamie Chu[1], Bhavya Sabbineni[1], Haoning Howard Cen[1], Xiaoke Hu[1], WenQing Grace Sun[1], George P. Brownrigg[1], Yi Han Xia[1], Jason Rogalski[2], James D. Johnson[1#]

Affiliations: [1] Department of Cellular and Physiological Sciences, Life Sciences Institute, University of British Columbia and the Vancouver Coastal Health Research Institute, Vancouver, Canada.
[2] Proteomics and Metabolomics Core Facility, Life Sciences Institute, University of British Columbia, Vancouver, Canada.

[#]**Address correspondence to**: James D. Johnson, PhD., 5358 Life Sciences Building, 2350 Health Sciences Mall, University of British Columbia, Vancouver, Canada, V6T 1Z3
Phone: 604 822 7187, Email: James.d.johnson@ubc.ca, Twitter: @JimJohnsonSci

Abstract

Pancreatic β cells exist in low and high insulin gene activity states that are dynamic on a scale of hours to days. Here, we used live 3D imaging, mass spectrometry proteomics, and targeted perturbations of β cell signaling to comprehensively investigate *Ins2*(GFP)^{HIGH} and *Ins2*(GFP)^{LOW} β cell states. We identified the two *Ins2* gene activity states in intact isolated islets, and cells in the same state were more likely to be nearer to each other. We report the proteomes of pure β cells to a depth of 5555 proteins and show that β cells with high *Ins2* gene activity had increased mRNA processing factors, as well as increased translation. We identified activators of cAMP signaling (GLP1, IBMX) as powerful drivers of transitions from *Ins2*(GFP)^{LOW} to the *Ins2*(GFP)^{HIGH} states. Okadaic acid and cyclosporine A had the opposite effects. This study provides new insight into the proteomic profiles and regulation of β cell states.

Keywords: insulin production; cellular heterogeneity; live cell imaging; single cell RNA sequencing; proteomics; fluorescence activated cell sorting

Introduction

Diabetes is characterized by dysfunctional glucose homeostasis which is caused by a relative (type 2 diabetes) or near-absolute (type 1 diabetes) deficiency in insulin, the body's main anabolic hormone (1). Insulin is produced by pancreatic islet β cells, whose dysfunction and/or death are prerequisites for diabetes progression (2-4). Not all β cells are the same (5-7). Several studies have shown that insulin content and mRNA can vary greatly between individual β cells (8; 9). Previously, live cell imaging using a dual *Ins1* and *Pdx1* fluorescent promoter reporter showed that mouse and human β cell lines could transition from less to more mature states (10; 11) and identified endogenous and chemical regulators of this process (12; 13). However, reporter constructs using abbreviated promoter fragments may not accurately report endogenous gene activity. Therefore, we used *Ins2*^{GFP} knock-in mice (14) to investigate endogenous *Ins2* gene activity and identified two distinct β cell states, one with high insulin gene activity and higher insulin mRNA, *Ins2*(GFP)^{HIGH}, and one with lower insulin gene activity and lower insulin mRNA, *Ins2*(GFP)^{LOW} (15). Live cell imaging revealed that β cells had the capacity to transition between the high and low GFP states in both directions (15). Single cell RNA sequencing (scRNAseq) demonstrated *Ins2*(GFP)^{HIGH} cells had a more mature β cell transcriptome profile, including

upregulation of factors related to optimal insulin secretion (15). However, it has been shown that the transcriptome and proteome have weak correlation in islets (16), so it is critical to understand the proteomic profile of these states. It is also important to understand the molecular mechanisms that control β cell state transitions. ER stress and other cellular perturbations are also known to impact gene transcription (17; 18). For example, stresses associated with the high *Ins2* state lead to β cell fragility (15) and lower proliferation capacity (19), but the effects of stress itself on *Ins2* gene activity remains unclear. With robotic imaging technology and automated analysis, it is possible to study dozens of signaling pathways at once.

Live imaging of β cell states also presents the opportunity for fluorescence activated cell sorting (FACS) purification of selected cell populations, while advances in mass spectroscopy permit the identification and cataloguing of thousands of cell-selective proteins that could be effects markers or targets for drug delivery. Previous proteomic studies purified β cells using insulin immunofluorescence staining or FAD autofluorescence (20; 21), but these methods for enriching β cells have caveats such as the reliance on antibody specificity and that FAD autofluorescence may not identify all β cells. Thus, there is need to revisit this approach with updated and more sensitive proteomics equipment and analysis pipelines.

Here, we define the proteomic profiles of purified rodent β cells and of the two *Ins2* gene activity states using *Ins2*^{GFP} knock-in mice. We also systematically tested the effects of 48 drugs known to affect selected signaling pathways and cellular functions on *Ins2* gene activity and β cell state transitions. We present the first comprehensive comparison of the two *Ins2* expression states at the protein and functional level, and reveal multiple genes implicated in mechanisms related to *Ins2* gene activity and β cell state transitions.

Methods

Animal husbandry and breeding

Animals were housed in the Modified Barrier Facility at UBC, under protocols approved by the UBC Animal Care Committee in accordance with national and international guidelines. To maintain consistency with our prior study (15) and to keep the genotype as close to wild-type as possible, all mice in this study were *Ins2*$^{WT/GFP}$ heterozygous mice. Including the *Ins1* gene, these mice have 3 out of 4 wildtype insulin alleles. Mice used for islet isolations were between 60 and 65 weeks of age.

Islet isolation and dissociation

Pancreatic islets were isolated using collagenase when mice were aged 60 weeks, filtered, and hand-picked as previously described (22). Islets were cultured overnight (37°C, 5% CO2) in RPMI1640 medium (ThermoFisher, Waltham, United States) with 11 mM glucose (Sigma), 100 units/ml penicillin, 100 µg/ml streptomycin (ThermoFisher, Waltham, United States), and 10% vol/vol fetal bovine serum (FBS; ThermoFisher, Waltham, United States). For islet dissociation, islets were washed 4 times with minimum essential medium (Corning, Corning, United States) and immersed for 5 minutes in 0.05% trypsin at 37°C with pipetting. Cells were then resuspended in RPMI1640 medium, plated in appropriate reservoirs or plates, and rested for 24 hours (37°C, 5% CO2)**.** Cells were incubated for 2 hours in the presence of 0.05 µg/mL Hoechst 33342 (Sigma–Aldrich, St. Louis, United States) to mark nuclei and 0.5 µg/mL propidium iodide (Sigma–Aldrich, St. Louis, United States) to mark cell death. Drug/small molecules for the perturbation study were purchased from the sources indicated in Table 2 and applied immediately prior to imaging.

Fluorescence-activated cell sorting

Pancreatic islets were dispersed using 0.05% trypsin and resuspended in 1x PBS with 0.005% FBS. Dispersed islets were then filtered into 5 ml polypropylene tubes. Sorting was conducted on a Cytopeia Influx sorter (Becton Dickinson, Franklin Lakes, USA) at the Life Sciences Institute FLOW core facility. Cells were excited with a 488 nm laser (530/40 emission) and a 561 nm laser (610/20 emission).

Live cell imaging and analysis

For 3D live imaging, intact mouse islets were incubated overnight in culture media (RPMI1640 medium with 11 mM glucose, 100 units/ml penicillin, 100 µg/ml streptomycin, and 10% vol/vol FBS) with Hoechst 33342 (0.05 µg/mL) and propidium iodide (0.5 µg/mL). After 24 hours, cells were transferred into 2 well or 8 well µ-Slides (Ibidi) with fresh culture media. Images were then acquired using a LEICA THUNDER Imager Live Cell & 3D assay microscope at 25x water objective (numerical aperture 0.95). Analysis of 3D live cell imaging experiments was done using Imaris Microscopy Image Analysis software with the FIJI Labkit module and custom R scripts. Image processing, including smoothing and background subtraction, was performed using Imaris. Labkit facilitated image labeling and pixel classification for the identification of GFP fluorescence in individual β cells. Nearest neighbor analysis was done using Imaris Python XTensions. Distance-to-core analysis was conducted on Imaris, using a reference frame positioned at the islet's center to measure the distance of each cell from the origin reference frame. Plots were generated for visualization using Graphpad Prism v10 or custom R scripts.

To investigate the effects of small molecules on GFP fluorescence, we cultured dispersed islet cells from *Ins2*^{GFP} mice on 384-well glass bottom plates (Perkin Elmer, Waltham, United States) and performed live cell imaging using an ImageXpress^{Micro} environmentally controlled, robotic system (Molecular Devices, San Jose, United States) which employed a 300 W Xenon lamp as previously described (15). Cells were stained with Hoechst 33342 and propidium iodide as described above. Images were acquired at 10x air objective, numerical aperture 0.3, at 30-minute intervals up to 96 hours, with cells being exposed to 359 nm light for 110 ms, 491 nm light for 15 ms, 561 nm for 75 ms. Analysis of live cell imaging experiments on *Ins2*^{GFP} cells was done using MetaXpress analysis software and custom R scripts. Tracking of GFP fluorescence in individual cells was performed as previously described (15). The *Ins2*(GFP)^{HIGH} and *Ins2*(GFP)^{LOW} subpopulations were identified using model-based clustering (23).

Protein synthesis assay

One day after isolation, dispersed islets were seeded into an optical 96-well plate (Perkin Elmer, Waltham, United States) at a density of approximately 16,000 cells per well in culture media (RPMI1640 medium with 11 mM glucose, 100 units/ml penicillin, 100 µg/ml streptomycin, and 10% vol/vol FBS). Treatments were applied 3 hours after seeding. After 24 hours of incubation, fresh culture media was applied, then supplemented with 20 µM OPP (Invitrogen, Waltham, United States). The assay was performed according to instructions provided by the manufacturer. Cells were imaged at 10x, numerical aperture 0.3, with an ImageXpress^{Micro} high-content imager and analyzed with MetaXpress to quantify the integrated staining intensity of OPP-Alexa Fluor 594 in cells identified by NuclearMask Blue Stain.

Mass Spectrometry / Proteomics

For proteomics sample preparation, between 2,000 and 10,000 cells were diluted with ultrapure water, and then lysed by adding cold trifluoroethanol (TFE) (final 50% TFE) to the suspension. Samples were then chilled on ice for 10 min, vortexed for 1 min and further sonicated for 5-10 min in an ice bath. Tris (pH 8-8.5) was added to adjust the pH and concentration to final 100 mM Tris at

pH 8-8.5. Total protein mass was estimated to be 0.3 ng/cell. Samples were reduced with tris(2-carboxyethyl)phosphine (1 µg TCEP: 50 µg protein) incubated for 20 min at room temperature, then alkalized with chloroacetamide (5 µg CAA:50 µg protein) incubated at 95 °C for 10 min. Then samples were diluted with 50mM Ammonium bicarbonate (final TFE < 10%). Proteins were digested with LysC/Trypsin (1 µg LysC/Trypsin: 50 µg protein) for 2 hours at 37 °C, followed by digestion with trypsin (1 µg trypsin: 50 µg protein) and incubated overnight at 37 °C. Samples were further digested with trypsin (1 µg trypsin: 125 µg protein) for 5 hours at 37 °C. Digestion was stopped by acidification. Samples were desalted with 6 mm depth of C18; briefly, STAGE (stop and go extraction) tips were conditioned with 100% methanol, equilibrated with 0.2% TFA, loaded with samples, then washed with 0.2% TFA, and finally eluted with 80 µL *2 of 40% ACN, 0.1% formic acid. Eluate was dried in vacuum then kept in -20°C. Before instrumental analysis, samples were reconstituted in in 0.5% acetonitrile, 0.1% formic acid and concentration was measured using NanoDrop One (ThermoFisher, Waltham, USA) with the A205 Scopes method (absorbance at 205 nm, baseline correction at 340 nm).

For liquid chromatography steps, 75 ng of peptides were injected and separated on-line using NanoElute UHPLC system (Bruker Daltonics Billerica, United States) with Aurora Series Gen2 (CSI) analytical column, (25 cm x 75 µm 1.6µm FSC (fuse silica core) C18, with Gen2 nanoZero and CSI (captive spray interface) fitting; Ion Opticks, Parkville, Australia) heated to 50 °C and coupled to timsTOF Pro (Bruker Daltonics, Billerica, USA). A standard 30 min gradient was run from 2% buffer B to 12% buffer B over 15 min, then to 33% B from 15 to 30 min, then to 95% B over 0.5 min, and held at 95% B for 7.72 min. Before each run, the analytical column was conditioned with 4 column volumes of buffer A. Where buffer A consisted of 0.1% aqueous formic acid and 0.5 % acetonitrile in water, and buffer B consisted of 0.1% formic acid in 99.4% acetonitrile. The NanoElute thermostat temperature was set at 7 °C. The analysis was performed at 0.3 µL/min flow rate.

For mass spectrometry steps, the Trapped Ion Mobility – Time of Flight Mass Spectrometer (TimsTOF Pro; Bruker Daltonics, Billerica, USA) was set to Parallel Accumulation-Serial Fragmentation (PASEF) scan mode for DIA acquisition scanning 100 – 1700 m/z. The capillary voltage was set to 1800V, drying gas to 3 L/min, and drying temperature to 180°C. The MS1 scan was followed by 17 consecutive PASEF ramps containing 22 non-overlapping 35 m/z isolation windows, covering the m/z range 319.5 – 1089.5 (more information in DIA windows). As for TIMS setting, ion mobility range (1/k0) was set to 0.70 – 1.35 $V{\cdot}s/cm^2$, 100 ms ramp time and accumulation time (100% duty cycle), and ramp rate of 9.42 Hz; this resulted in 1.91s of total cycle time. The collision energy was ramped linearly as a function of mobility from 27 eV at 1/k0 = 0.7 $V{\cdot}s/cm^2$ to 55 eV at 1/k0 = 1.35 $V{\cdot}s/cm^2$. Mass accuracy: error of mass measurement is typically within 3 ppm and is not allowed to exceed 7 ppm. TimsTOF Pro was run with timsControl v. 4.1.12 (Bruker, Billerica, USA). LC and MS were controlled with HyStar 6.0 (6.2.1.13, Bruker, Billerica, United States). For the final search and quantification of the results, acquired diaPASEF data were then searched using DIA-NN (v. 1.8.1) to obtain DIA quantification, with the spectral library generated from the canonical proteome for *Mus Musculus* from UniProt. Quantification mode was set to “Any LC (high precision) and a two-pass search was completed. All other settings were left default. Mice with a GFP protein ratio of less than 3 when comparing their respective *Ins2*(GFP)^{HIGH} and *Ins2*(GFP)^{LOW} samples were excluded.

Statistics and data visualization

Statistics and data representation for nearest neighbor analyses, distance to core analyses, and OPP translation assays, were conducted using GraphPad Prism v10 (GraphPad Software, San Diego, USA). Statistics and data representation for live cell imaging experiments employed custom

R scripts. Student's t-test and one-way ANOVAs were used for parametric data as indicated in figure legends. For all statistical analyses, differences were considered significant if the p value was less than 0.05. Error bars were presented as ± standard error of the mean (SEM).

For proteomics analyses, proteins that were present in less than 80% of samples were removed from analysis. Significantly differential proteins were defined with a threshold of p value < 0.05 and a fold-change of more than 20%, and graphs were generated using custom R scripts. For STRING and Cytoscape analyses, significantly differentially abundant proteins were entered into the STRING website, where nodes and networks were generated. For STRING settings, only 'Experiments' and 'Databases' interactions were included, with medium confidence interaction scores. STRING networks and protein expression data were then imported into Cytoscape and reordered according to their cellular location. Background images were generated with Biorender.

For STRING and Cytoscape analyses in our small molecule screen, the primary binding proteins for small molecules were determined using online literature search. Proteins were then entered into STRING, where nodes and networks were rendered. For settings on STRING, all interactions were included, with medium confidence interaction scores. STRING networks, GFP fluorescence, cell death, and cell state transition data were then imported and finalized in Cytoscape. Background graphs were generated using Biorender.

Results

Live 3D imaging of intact islets from *Ins2*^{GFP} mice

Our previous analyses of *Ins2* gene activity in dispersed mouse islets revealed a bimodal distribution of GFP fluorescence from a reporter construct knocked into the endogenous *Ins2* gene locus (15) (Fig. 1A, B). In this study, we used live 3D imaging to define the prevalence and spatial relationship of cells in the two β cell insulin gene activity states in whole intact islets from *Ins2*^{GFP} knock-in mice (Fig. 1C). We analyzed islets which had below 400 GFP positive cells, as we wanted to avoid large islets which may have necrotic cores (24). Consistent with dispersed cells, *Ins2* gene activity in intact islets also had a bimodal distribution (Fig. 1D). We also found that the range of GFP fluorescence was greater in larger islets compared to smaller ones (Fig. 1D). We did not find significant sex differences when comparing the ratios of *Ins2*(GFP)^{HIGH} and *Ins2*(GFP)^{LOW} cells in intact male and female islets (Fig. 1E), consistent with our previous work in dispersed β cells (22). Nearest neighbor analysis showed that cells in the same *Ins2* activity state were more likely to be found in proximity of each other (Fig. 1F; Supplemental Fig. 1A). We found no significant difference between the cell states and their distance to the core of the islet (Fig. 1G; Supplemental Fig. 1B). To summarize, live cell 3D imaging analysis revealed the that the *Ins2*(GFP)^{HIGH} and *Ins2*(GFP)^{LOW} expression states exist in intact islets, with cells in the same expression states being more likely to be found next to each other.

Identification of β cell selective islet proteins

Proteins that are selective to β cells have potential as biomarkers and anchor targets for imaging and drug delivery (25). Previous studies have identified β cell-specific mRNAs using single cell RNA sequencing (26). However, mRNA and proteins in isolated islets only have a correlation coefficient of ~0.5 (16), so there is an unmet need for minimally biased, high-throughput characterization of β cell selective gene products at the protein level. Therefore, as a step towards identifying β cell specific proteins, we compared the proteomes of GFP positive cells to GFP negative cells from dispersed and sorted mouse islets to a depth of 5555 proteins (Fig. 2A; Supplemental Fig. 2A, 3A). As expected, GFP-negative, non-β cells were enriched for known

markers of other islet cell types, such as GCG, PYY, and PPY (Fig. 2A). To rank the proteins, we multiplied the p-value by the fold change. The top novel non-β cell proteins were the cell surface protein tetraspanin 8 (TSPAN8), arginase 1 (ARG1), and clusterin (CLU) (Fig. 2A). The top 5 most significantly enriched β cell selective proteins were: 1) CAP-Gly domain containing linker protein 1 (CLIP1), which links cytoplasmic vesicles to microtubules; 2) 3'-phosphoadenosine 5'-phosphosulfate synthase 2 (PAPSS2), which mediates two steps in the sulfate activation pathway; 3) tyrosine 3-monooxygenase/tryptophan 5-monooxygenase activation protein zeta (YWHAZ), also known as 14-3-3ζ, a scaffolding protein we have shown plays important survival and signaling roles in β cells (27); 4) apoptosis inducing factor mitochondria associated 1 (AIFM1); and 5) cystathionine beta synthase (CBS), a gene which may play a role in β cell insulin secretion (28) (Fig. 2A). As expected, INS1 and IAPP proteins were also significantly enriched in pure β cells. The G protein-coupled receptor 158 (GPR158), a metabotropic glycine receptor (29) which may play a role in autocrine feedback (30), was highly enriched in β cells.

We next undertook pathway analysis to identify themes in our proteomic data from non-β cells and pure β cells (Fig. 2C). Gene set enrichment analyses revealed that non-β cells are enriched for proteins that mediate metabolic and catabolic processes including 'cellular modified amino acid metabolic process' and 'carbohydrate derivative metabolic process'. In pure β cells, there was enrichment of pathways entitled 'skin development' and 'supramolecular fiber organization', which was driven by the relative abundance of multiple keratin family proteins, which are known to modulate β cell signalling and play roles in stress responses (31). Enrichment of 'regulation of cellular component biogenesis' and 'regulation of protein-containing complex assembly' pathways suggests β cells may exist in a more anabolic state than non-β cells. Pathways involving 'protein phosphorylation' and 'IκB/NFκB signalling' were also enriched in pure GFP-positive β cells (Fig. 2C). Interestingly, NFκB signalling has been implicated in a β cell subpopulation with lower PDX1 expression, which has similarities with our *Ins2*(GFP)^{LOW} cells (32). Overall, these results suggest that differences between *Ins2* expressing cells and other islet cells are primarily associated with protein production and signalling.

Proteomic profiles of FACS purified β cells in *Ins2*(GFP)^{HIGH} and *Ins2*(GFP)^{LOW} states

We next compared the proteomic profiles of the two distinct *Ins2* gene activity states in FACS purified β cells (Fig. 2B, Supplemental Fig. 2A, 3B). Using p value times fold change as a criteria again, the top 5 most enriched proteins in *Ins2*(GFP)^{LOW} cells were: 1) glucagon (GCG), a marker for alpha cells; 2) pancreatic polypeptide (PPY) a marker for PP cells; 3) Purkinje cell protein 4 (PCP4), a calmodulin regulator involved in calcium binding and signalling; 4) aldehyde dehydrogenase 1 family member 3 (ALDH1L2), a mitochondrial enzyme implicated in β cell protection and secretory dysfunction (33); and 5) adenine phosphoribosyltransferase (APRT), an enzyme involved in the nucleotide salvage pathway (Fig. 2B). These results suggest that cells in the less mature *Ins2*(GFP)^{LOW} state was enriched in markers of 'multi-hormonal' cells, consistent with our previous scRNAseq analysis (15). We also found enrichment in proteins in endoplasmic reticulum processing, including HSPA5, HSP90B1, and ERO1L (Supplemental Fig. 4A-C), corroborating our prior scRNAseq analyses(15).The top 5 most enriched proteins (other than GFP) in *Ins2*(GFP)^{HIGH} cells were: 1) zinc finger AN1-type containing 2B (ZFAND2B), a protein associated with the proteasome for degradation of misfolded proteins; 2) zinc finger RANBP2-type containing 2 (ZRANB2), a protein involved in RNA splicing and mRNA processing 3) myocyte enhancer factor 2D (MEF2D), a calcium regulated transcription factor; 4) SWI/SNF related, matrix associated, actin dependent regulator Of chromatin subfamily A, member 2 (SMARCA2), a protein which regulates transcription via altering chromatin structure; and 5) phosphofurin acidic cluster sorting protein 2 (PACS2), a protein involved in ER calcium ion homeostasis. The protein poly(A)

polymerase alpha (PAPOLA), a protein required for creation of the 3'-poly(A) tail of mRNAs, was also upregulated in *Ins2*(GFP)^{HIGH} cells (Fig. 2B; Supplemental Fig. 3B).

The pathways significantly enriched in the *Ins2*(GFP)^{LOW} state relative to the *Ins2*(GFP)^{HIGH} state included: 'organic acid metabolic process', 'cellular respiration', 'generation of precursor metabolites and energy', and 'oxidative phosphorylation', suggesting the less mature cells may have more energic capacity. They are also enriched in proteins involved in 'fatty acid metabolic processes' and 'lipid metabolic processes', suggesting the possibility of metabolic substrate preference and switching between these cell states (Fig. 2D). The *Ins2*(GFP)^{LOW} state was enriched in 'hormone metabolic process' which was also enriched in non-β cells relative to β cells, including GCG, PYY, and SST. Gene set enrichment analysis revealed that the pathways most enriched in the *Ins2*(GFP)^{HIGH} state were related to transcriptional upregulation and mRNA processing (Fig. 2D). The upregulation of 'DNA-templated transcription' and 'RNA biosynthetic process' pathways may suggest that the *Ins2*(GFP)^{HIGH} state is more transcriptionally active. The *Ins2*(GFP)^{HIGH} state also enriched for 'RNA processing', a pathway which involves mRNA capping and addition of the 3'poly(A) tail. Regulation and processing of the 5' and 3' UTRs of insulin mRNA is known for their importance in maintaining mRNA stability, and our prior scRNAseq and qPCR data indeed showed that the *Ins2*(GFP)^{HIGH} state had more *Ins2* mRNA (15). 'Chromosome organization' and 'cell cycle' pathway upregulation is also indicative of regulation of the transcriptional landscape. Overall, this data suggests that differences between the *Ins2*(GFP)^{HIGH} and *Ins2*(GFP)^{LOW} states were related to transcription mechanisms and processes.

We next analysed the relationship between our differentially abundant proteins using STRING and mapped them to a cell diagram in Cytoscape to visualize protein-protein networks in their most common cellular locations (Fig. 3A, B). Protein-protein interaction networks enriched in GFP negative cells, beyond the known markers from other islet cell types (GCG, PYY, PPY, SST), included protein networks related to lipid metabolism (GPX3, HEXB) and factors related to amino acid synthesis and transport (SLC7A8, SLC3A2, ARG1) (Fig. 3A). Protein-protein interaction networks enriched in GFP positive cells, compared with non-GFP, included those involved in GPCR and cAMP signalling, glycolysis, and the secretory pathway (ER, Golgi, granules, cytoskeleton). Specifically, pure β cells showed enrichment for multiple cytoskeletal factors, including VIL1, a member of calcium regulated actin binding proteins and is known plays a role in insulin exocytosis regulation; and CLIP1, a protein associated with granule trafficking (34-36). These data provide data on β cell specific protein networks at unprecedented detail.

Next, we examined network differences between the *Ins2*(GFP)^{HIGH} state and the *Ins2*(GFP)^{LOW} state. The *Ins2*(GFP)^{LOW} state was enriched for networks related to mitochondria function and cell respiration, including members of the pyrroline-5-carboxylate reductase family (PYCR1, PYCR2), and subunits of the NADH dehydrogenase (ubiquinone) complex (NDUFA6, NDUFB6, NDUFB10) (Fig. 4A). We also noted a number of factors with links to proteasome function (PSMA3, PSMB3, PSMB8), and translation factors (EIF3BEIF4E, EIF4A1) (Fig. 4A). This suggests that cells with low *Ins2* gene activity may be recovering from various sources of stress and may also be in the process of regulating translation machinery. Interestingly, RHOA, an F-actin regulator which reduces insulin secretion when activated, was upregulated in the *Ins2*(GFP)^{LOW} state (37). Another actin protein, ARPC2, which was downregulated in human islets when treated with insulin, was also enriched in *Ins2*(GFP)^{LOW} cells (38). On the other hand, many of the enriched proteins in the *Ins2*(GFP)^{HIGH} state were located in the nucleus and were linked to transcriptional regulation, including prominent transcription factors TOP1, CDK9, and KAT7(Fig. 4B). Several nuclear proteins were associated with mRNA processing, such as ZRANB2, SRPK1, and PAPOLA (39-41) (Fig. 4B). We also noted a number of factors in the Golgi, including STRIP1, a protein involved in the localization of the Golgi, and VCPIP1, a protein involved in Golgi reassembly. There were also

a fair number of proteins in the ER, including the aforementioned ZFAND2B and PACS2; DNAJA1, a protein which stimulates ATP hydrolysis; and NGLY1, an enzyme involved in the degradation of misfolded proteins. Taken together, the *Ins2*(GFP)^{HIGH} state is primarily associated with the regulation of transcription, mRNA processing, and protein trafficking, while the *Ins2*(GFP)^{LOW} state may be in the process of recovering from stress associated with high *Ins2* gene activity and a shift in protein translation machinery.

Our proteomics data revealed enrichment of 'regulation of cellular component biogenesis' and 'regulation of protein-containing complex assembly' pathways in the *Ins2*(GFP)^{HIGH} state, so we tested whether β cell translation capacity was different compared to other islet cell types using the O-propargyl-puromycin (OPP) assay, which incorporates a fluorescent marker into nascent proteins (Fig. 5A). Using GFP as a marker for β cells, we found that β cells had higher translational capacity compared to other islet cells (Fig. 5B). The upregulation of DNA template transcriptional regulation and RNA processing pathways in *Ins2*(GFP)^{HIGH} cells relative to *Ins2*(GFP)^{LOW} cells is suggestive of increased downstream translational capacity. We found that cells in the *Ins2*(GFP)^{HIGH} state had significantly higher translational capacity compared to cells in the *Ins2*(GFP)^{LOW} state (Fig. 5C, D). We did not note any significant differences when comparing the translational capacity of the two *Ins2* expression states in the context of sex differences (Supplemental Fig. 6A). Overall, these data reveal the differences between the *Ins2*(GFP)^{HIGH} and *Ins2*(GFP)^{LOW} expression states at the protein level, and show how some of these differences can translate to differences in β cell function.

Mechanistic interrogation of *Ins2* gene activity regulation

The molecular mechanisms regulating *Ins2* gene activity are not clear. We chose 48 drugs known to perturb key β cell signaling pathways to study their regulation of β cell states (Table 2)(Fig. 6A). Concentrations for the various compounds were decided based on documented doses used in *in vitro* assays. Dispersed islet cells from *Ins2*^{GFP} mice were treated with compounds and imaged in a high-throughput format (Fig. 6B-L). Although all of the experiments were conducted in parallel using a robotic imaging system, we visualized the results from each family of compounds separately. Compounds which activate cAMP signalling, namely the PDE inhibitor 3-isobutyl-1-methylxanthine (IBMX) and the cAMP inducer GLP-1, significantly increased *Ins2* gene activity when tracked over time (Fig. 6B). The rate of increase for GFP fluorescence was considerably greater in *Ins2*(GFP)^{HIGH} cells in response to cAMP pathway activators compared to *Ins2*(GFP)^{LOW} cells (Fig. 7B, C). Compared to DMSO control, the calcineurin pathway inhibitors cyclosporine A, okadaic acid, and tacrolimus reduced *Ins2* gene activity (Fig. 6C). Inhibitors of the endonuclease IRE1A caused a steep drop in *Ins2* gene activity after prolonged treatment, with APY29 inducing a strong increase prior to the drop (Fig. 6D). Effectors of ER pumps and channels had relatively few effects on *Ins2* gene activity, with ATP2A2 inhibitor thapsigargin slightly increasing *Ins2* activity (Fig. 6E). Compounds which impacted insulin signalling also had some interesting effects, in particular the protein kinase inhibitor staurosporine, which significantly increased *Ins2* gene activity, and PI3K inhibitor LY294002, which caused a spike at 48 hours followed by a steep decline (Fig. 6F). The glucocorticoid agonist dexamethasone reduced *Ins2* activity, while PPARG agonist rosiglitazone slightly increased it (Fig. 6G). The three nutrients we tested all increased *Ins2* gene activity, with arginine and sodium butyrate having a more significant increase over time compared to palmitic acid (Fig. 6H). Compounds which affected cell membrane excitability also had interesting effects, with K_{ATP} channel (ABCC8 subunit) activator diazoxide and CACNA1C inhibitor verapamil decreasing *Ins2* gene activity, while K_{ATP} channel (ABCC8 subunit) inhibitor tolbutamide modestly increased it near the end of our experiment (Fig. 6I). Perturbing protein degradation factors also yielded effects, in particular ERAD inhibitor eeyarestatin I, which decreased *Ins2* gene

activity rapidly after treatment (Fig. 6J). As expected, many compounds which affected transcriptional machinery also impacted *Ins2* gene activity (Fig. 6K). TFIIH inhibitor Triptolide and RNA polymerase II inhibitor alpha amanitin resulted in an increase in *Ins2* activity, peaking at around 48 hours and rapidly declining afterwards (Fig.6K). CDK9 inhibitor 5, 6-dichloro-1-β-D-ribofuranosylbenzimidazole (DRB) also increased *Ins2* gene activity (Fig. 6K). TOP1 inhibitor actinomycin D caused a steep decline in *Ins2* gene activity 24 hours after treatment (Fig. 6K). HDAC inhibitors MGCD0103 and trichostatin A both reduced *Ins2* gene activity, but not as abruptly as triptolide and alpha amanitin (Fig. 6K). Compounds which affected translation that had an effect on *Ins2* gene activity include EEF2 inhibitor cyclohexamide, which increased *Ins2* activity followed by a steep decline after 48 hours, PKR inhibitor, which increased *Ins2* gene activity, and PERK activator CCT020312 and EIF2S1 inhibitor sal003, which reduced *Ins2* gene activity (Fig. 6L).

We performed hierarchical clustering using various cell behavior traits in the context of comparing cells from male and female mice (Supplemental Fig. 5A,B). Cell activity traits we used included mean GFP (average GFP fluorescence over time), max GFP (peak GFP fluorescence), and mean cell death (average PI intensity). Overall, the strongest effectors of GFP fluorescence did not show any significant sex differences (Supplemental Fig. 5A).

Rapid drops in GFP fluorescence are indicative of cell death, so we explored the relationship between GFP expression and cell viability by plotting fluorescence in the green wavelength (GFP) against the red wavelength (PI) (Fig. 6M) (15). We note that the cAMP agonists IBMX and GLP-1 amide had the highest GFP fluorescence with relatively low cell death (Fig. 6M). We found that okadaic acid and trichostatin A had the greatest decrease in GFP fluorescence without significant cell death (Fig. 6M). The subset of drugs which had increasing GFP fluorescence followed by a rapid drop (APY 29, triptolide, alpha amanitin, cyclohexamide, DRB, LY294002) had significant cell death, indicating the drugs were toxic after prolonged treatment (Fig. 6M). This is supported by an OPP assay done in the context of several small molecules of interest (GLP-1 amide, IBMX, APY 29, triptolide), in which a significant drop in translational capacity can be observed after 24 hours of treatment, well before the drop in GFP fluorescence and noticeable cell death (Supplemental Fig. 6B). Overall, our small molecule screen shows how various drugs and small molecules may impact *Ins2* gene activity and how it may correlate to β cell health.

Cell state transitions in the context of media conditions and perturbations

Various culture conditions can impact cell state transitions, with higher glucose concentrations and the addition of FBS inducing a greater rate of *Ins2*(GFP)^{LOW} to *Ins2*(GFP)^{HIGH} transitions (Fig. 7A). We next analyzed the rate of transitions for cells from *Ins2*^{GFP} knock-in mice in the context of our small molecule screen (Fig. 7D). In general, most small molecules had higher *Ins2*(GFP)^{HIGH} to *Ins2*(GFP)^{LOW} transitions rates compared to *Ins2*(GFP)^{LOW} to *Ins2*(GFP)^{HIGH}, with our DMSO control at possessing a ~3:1 ratio (9.1% *Ins2*(GFP)^{HIGH} to *Ins2*(GFP)^{LOW}, 3.2% *Ins2*(GFP)^{LOW} to *Ins2*(GFP)^{HIGH}). Compared to our DMSO control, we found that cAMP agonists GLP-1 amide and IBMX had the greatest increase in *Ins2*(GFP)^{LOW} to *Ins2*(GFP)^{HIGH} transitions (19% for GLP-1 amide, 14% for IBMX), with relatively low levels of *Ins2*(GFP)^{HIGH} to *Ins2*(GFP)^{LOW} transitions (Fig. 7B-D). Okadaic acid and cycplosporin A induced the highest rate of *Ins2*(GFP)^{HIGH} to *Ins2*(GFP)^{LOW} transitions (Fig. 7D). Interestingly, we found that several drugs with high GFP, including triptolide, APY 29, and alpha amanitin, had very few transitions of either type (Fig. 7D). This shows that the increase in GFP fluorescence observed in these treatments was primarily driven by increasing GFP fluorescence in the *Ins2*(GFP)^{HIGH} cells, and not in the *Ins2*(GFP)^{LOW} cells.

STRING/Cytoscape analyses helped contextualize the major binding partners of our small molecule screen (Fig. 8A). Several of the strongest effectors of GFP fluorescence were found to impact genes located within the nucleus, including CDK9, TOP1, POL2A, ERCC3, HDAC1,

HDAC2, SP1, and PAK1. Many of these proteins have known roles in transcriptional mechanisms (42-47). On the membrane, GLP1R and NOS1 were receptors which had effects on GFP fluorescence. In the ER, perturbing ERN1, a major factor in UPR response, impacted GFP fluorescence and cell health (48). In the cytosol, perturbation of VCP, a major component of ERAD, resulted in heavy cell death, while PIK3CA, PDE3A, EEF2 influenced GFP fluorescence. In the context of cell state transitions, perturbing PDE3A and GLP1R induced the highest rate of *Ins2*(GFP)^{LOW} to *Ins2*(GFP)^{HIGH} transitions, while perturbing PPP3CC and PPP2CA resulted in the highest rate of *Ins2*(GFP)^{HIGH} to *Ins2*(GFP)^{LOW} transitions. Overall, these results show how perturbing various β cell signalling pathways may impact *Ins2* gene activity and cell state transitions.

Discussion

This study aimed to further our understanding of dynamic *Ins2* gene activity states, their proteomic profiles, and their regulation by key cellular processes. Our 3D imaging experiments showed how the *Ins2*(GFP)^{HIGH} and *Ins2*(GFP)^{LOW} expression states existed in live intact islets. The two *Ins2* gene expression states were present in intact islets. We did not find any correlation for either cell population to the islet periphery or core. This is similar to what was observed by Johnston *et al*, in which hub cells, a β cell sub-set with similarities to *Ins2*(GFP)^{LOW} cells, did not show any clear preference for the islet center or periphery (49). Interestingly, cells in the same expression states were more likely to be next to each other, forming patches cells. In future experiments, it would also be interesting to investigate the spatial dynamics of the two cell states and their relationship with other cells (50; 51).

Our study characterized the *Ins2*(GFP)^{HIGH} and *Ins2*(GFP)^{LOW} expression states at the proteome level and revealed mechanisms governing *Ins2* gene activity and cell state transitions. Minimally biased interrogation of proteins and protein networks selectively present in β cells and β cell states builds on past efforts to map the β cell proteome. Previously established FACS purifying mouse β cell populations based on insulin immunoreactivity yielded 6955 proteins across 36 islet samples with various diets and islet cell types (20), and led to the identification of a subpopulation of β cells with low CD81 expression which had enrichment for factors in spliceosome and RNA processing pathways, but reduced oxidative phosphorylation factors, similar to our *Ins2*(GFP)^{HIGH} cells (20). Two β cell subpopulations identified in a study on human β cell scRNAseq data had low *INS* expression, and while one high UPR marker expression, the other had enrichment in pathways related to oxidative stress (8). These two β cell subpopulations possess similarities with our *Ins2*(GFP)^{LOW} cells, which had upregulation in ER stress markers and metabolic processes (Supplemental Fig. 4A-C, Fig. 2D), and it was proposed that these low *INS* expressing cells were in a state of recovery from the various stresses of high insulin production (8). A recent study investigating younger and older insulin granules in INS-1 cells found proteins such as DYNC1H1, DCTN4, ARHGAP1 and EIF2S2 enriched in younger granules; these proteins were also significantly or trending towards enriched in *Ins2*(GFP)^{LOW} cells, suggesting that the two cell states may have different proportions of young and old insulin granules (52).. Overall, our study identifies novel and previously established β cell markers at the protein level and presented results showing how the cells in a high *Ins2* gene expression state had enrichment for factors related to RNA processing and transcription, with reduced oxidative phosphorylation and ER stress markers.

Our OPP protein translation assay revealed that the *Ins2*(GFP)^{HIGH} state had significantly more protein synthesis activity. This upregulation of translation could be mediated by increased abundance of mRNA processing proteins (such as PAPOLA and ZRANB2) and proteins which may

play a role in translation (such as DRG1 and ZC3H15) that were detected in proteomics (Fig. 4B). The increased translation may also suggest that these cells may represent a more “translationally active” population of cells, and not represent true *Ins2* gene activity. While we cannot fully rule out this possibility, our prior study showed that FACS purified *Ins2*(GFP)^{HIGH} cells did indeed have upregulated *Ins2* mRNA using qPCR (15). Furthermore, our scRNAseq data showed that *Ins2* mRNA was the most positively correlated gene with GFP mRNA (15). Future studies should look into whether this upregulation in translational capacity is indicative of enhanced insulin secretion capacity (7; 53; 54).

Our targeted perturbation analysis revealed pathways which impact endogenous *Ins2* gene activity and cell state transitions. The calcineurin inhibitors tacrolimus, cyclosporine A, and okadaic acid reduced *Ins2* gene activity (Fig. 6C), consistent with known roles for calcineurin on insulin mRNA in transgenic mice with a human insulin promoter (55). Okadaic acid and cyclosporine A are the two top inducers of *Ins2*(GFP)^{HIGH} to *Ins2*(GFP)^{LOW} transitions. NFAT, a calcineurin target, has been reported to be required for cAMP-mediated upregulation of insulin transcription in INS-1E cells (56). Interestingly, IRS2, a reported target of calcineurin for regulation of human β cell survival, is enriched in *Ins2*(GFP)^{HIGH} cells, further supporting a role for calcineurin in cell state regulation (57).

A key finding of our study was that GLP-1 amide and IBMX robustly increased *Ins2* activity over time, peaking at around 25 hours for GLP-1 amide and 55 hours for IBMX (Fig. 6B). This is consistent with previous data demonstrating that cAMP signaling plays a critical role in insulin production and secretion (58). Interestingly, GLP-1 and IBMX, also had the highest rates of *Ins2*(GFP)^{LOW} to *Ins2*(GFP)^{HIGH} transitions (Fig. 7D). Our proteomics analyses revealed that *Ins2*(GFP)^{HIGH} cells had upregulation in two phosphodiesterase (PDE) isoforms, PDE1C and PDE8A, both of which are known to play major roles in regulating cAMP and GSIS in rodent β cells (59; 60). Okadaic acid, the strongest inducer of *Ins2*(GFP)^{HIGH} to *Ins2*(GFP)^{LOW} transitions, is known to increase PDE expression in rat adipocytes (61). It is also worth noting that despite strongly upregulating GFP expression, many treatments including APY29, triptolide, alpha amanitin, staurosporine, sodium butyrate, and arginine, did not induce nearly as many cell state transitions as IBMX and GLP-1 amide. Taken together, these results may suggest that the dynamics between calcineurin, cAMP, and PDE concentrations play a major role in regulating *Ins2* gene activity and cell state transitions.

Some small molecules had effects on GFP fluorescence that were strongly correlated to cell health. For example, actinomycin D and eeyarestatin I killed cells rapidly upon treatment, resulting in a rapid collapse of GFP fluorescence. Interestingly, a subset of drugs including APY29 (IRE-1A inhibitor), triptolide (TFIIH inhibitor), alpha amanitin (RNA polymerase II inhibitor), cyclohexamide (EEF2 inhibitor), DRB (CDK9 inhibitor), and LY294002 (PI3K inhibitor) induced a strong increase in GFP fluorescence followed by rapid cell death after prolonged treatment. The endonuclease IRE-1A is an important factor in β cell stress regulation (48). Inhibition of general transcriptional machinery such as TFIIH and RNA polymerase II is highly detrimental to cell health after prolonged periods of time (62; 63). Inhibition of translation and cell cycle factors are also known to be toxic to cells (64; 65). The PI3K signalling pathway is linked to cell survival and resistance mechanisms (66)., The toxicity of these drugs may result in a buildup of stress cumulating in eventual cell death. It is interesting to note that the increase in GFP fluorescence in these drugs only occurs in *Ins2*(GFP)^{HIGH} cells, but not *Ins2*(GFP)^{LOW} cells. This may be due to the inherent fragility in *Ins2*(GFP)^{HIGH} cells, which may make them more vulnerable to the effects of stress (15). Autofluoresence is also known to increase during the process of cell death, and this may also contribute to the increase in GFP fluorescence (67). It is also worth noting that the two small molecules which induced the greatest increase in GFP fluorescence, GLP-1 amide and IBMX, are

also well known to have protective effects on β cells (68; 69). The OPP assay done in the context of several small molecules of interest also supports this, with cells treated to 24 hours of triptolide and APY 29 displaying reduced translational capacity prior to cell death and reduction in GFP fluorescence. These findings may suggest links between cell health and *Ins2* gene activity.

In summary, we provide data which further reveals the differences between the *Ins2*(GFP)^{HIGH} and *Ins2*(GFP)^{LOW} expression states beyond our previous study. Our live cell 3D imaging captures the two cell states in intact living islets, and our proteomic and translational assays characterizes them at the protein and functional level. The small molecule screen reveals pathways which may impact *Ins2* gene activity and cell state transitions, including prominent effects by effectors of cAMP signalling. Our study highlights the importance of cell expression states and cell state transitions in the islet, and how targeting factors which influence cell state transitions may help manage β cell function in diabetes.

References

1. Tisch R, McDevitt H: Insulin-dependent diabetes mellitus. Cell 1996;85:291-297
2. Boland BB, Rhodes CJ, Grimsby JS: The dynamic plasticity of insulin production in beta-cells. Mol Metab 2017;6:958-973
3. Butler AE, Janson J, Bonner-Weir S, Ritzel R, Rizza RA, Butler PC: Beta-cell deficit and increased beta-cell apoptosis in humans with type 2 diabetes. Diabetes 2003;52:102-110
4. Brozzi F, Eizirik DL: ER stress and the decline and fall of pancreatic beta cells in type 1 diabetes. Ups J Med Sci 2016;121:133-139
5. Avrahami D, Klochendler A, Dor Y, Glaser B: Beta cell heterogeneity: an evolving concept. Diabetologia 2017;60:1363-1369
6. Giselle Dominguez Gutierrez JGaLS: Heterogeneity of the Pancreatic Beta Cell. Frontiers in Genetics 2017;8:9
7. Dorrell C, Schug J, Canaday PS, Russ HA, Tarlow BD, Grompe MT, Horton T, Hebrok M, Streeter PR, Kaestner KH, Grompe M: Human islets contain four distinct subtypes of beta cells. Nat Commun 2016;7:11756
8. Xin Y, Dominguez Gutierrez G, Okamoto H, Kim J, Lee AH, Adler C, Ni M, Yancopoulos GD, Murphy AJ, Gromada J: Pseudotime Ordering of Single Human beta-Cells Reveals States of Insulin Production and Unfolded Protein Response. Diabetes 2018;67:1783-1794
9. Farack L, Golan M, Egozi A, Dezorella N, Bahar Halpern K, Ben-Moshe S, Garzilli I, Toth B, Roitman L, Krizhanovsky V, Itzkovitz S: Transcriptional Heterogeneity of Beta Cells in the Intact Pancreas. Dev Cell 2019;48:115-125 e114
10. Szabat M, Luciani DS, Piret JM, Johnson JD: Maturation of adult beta-cells revealed using a Pdx1/insulin dual-reporter lentivirus. Endocrinology 2009;150:1627-1635
11. Szabat M, Pourghaderi P, Soukhatcheva G, Verchere CB, Warnock GL, Piret JM, Johnson JD: Kinetics and genomic profiling of adult human and mouse beta-cell maturation. Islets 2011;3:175-187
12. Szabat M, Johnson JD, Piret JM: Reciprocal modulation of adult beta cell maturity by activin A and follistatin. Diabetologia 2010;53:1680-1689
13. Szabat M, Modi H, Ramracheya R, Girbinger V, Chan F, Lee JT, Piske M, Kamal S, Carol Yang YH, Welling A, Rorsman P, Johnson JD: High-content screening identifies a role for Na(+) channels in insulin production. R Soc Open Sci 2015;2:150306
14. Wakae-Takada N, Xuan S, Watanabe K, Meda P, Leibel RL: Molecular basis for the regulation of islet beta cell mass in mice: the role of E-cadherin. Diabetologia 2013;56:856-866
15. Chu CMJ, Modi H, Ellis C, Krentz NAJ, Skovso S, Zhao YB, Cen H, Noursadeghi N, Panzhinskiy E, Hu X, Dionne DA, Xia YH, Xuan S, Huising MO, Kieffer TJ, Lynn FC, Johnson JD: Dynamic Ins2 Gene Activity Defines beta-Cell Maturity States. Diabetes 2022;71:2612-2631

16. Kolic J SG, Cen HH, Ewald J, Beet L, Moravcova R, Rogalski JC, Sasaki S, Sun H, Rajesh V, Xia YH, Skovsø S, Spigelman AF, Fox JEM, Lyon J, Xia J, Lynn FC, Gloyn AL, Foster LJ, MacDonald PE, Johnson JD: Proteomic predictors of individualized nutrient-specific insulin secretion in health and disease. MedRxiv 2024:25
17. Hershey JW, Sonenberg N, Mathews MB: Principles of translational control: an overview. Cold Spring Harb Perspect Biol 2012;4
18. Spriggs KA, Bushell M, Willis AE: Translational regulation of gene expression during conditions of cell stress. Mol Cell 2010;40:228-237
19. Szabat M, Page MM, Panzhinskiy E, Skovso S, Mojibian M, Fernandez-Tajes J, Bruin JE, Bround MJ, Lee JT, Xu EE, Taghizadeh F, O'Dwyer S, van de Bunt M, Moon KM, Sinha S, Han J, Fan Y, Lynn FC, Trucco M, Borchers CH, Foster LJ, Nislow C, Kieffer TJ, Johnson JD: Reduced Insulin Production Relieves Endoplasmic Reticulum Stress and Induces beta Cell Proliferation. Cell Metab 2016;23:179-193
20. Fu Q, Jiang H, Qian Y, Lv H, Dai H, Zhou Y, Chen Y, He Y, Gao R, Zheng S, Liang Y, Li S, Xu X, Xu K, Yang T: Single-cell RNA sequencing combined with single-cell proteomics identifies the metabolic adaptation of islet cell subpopulations to high-fat diet in mice. Diabetologia 2023;66:724-740
21. Brackeva B, Kramer G, Vissers JP, Martens GA: Quantitative proteomics of rat and human pancreatic beta cells. Data Brief 2015;3:234-239
22. Brownrigg GP, Xia YH, Chu CMJ, Wang S, Chao C, Zhang JA, Skovso S, Panzhinskiy E, Hu X, Johnson JD, Rideout EJ: Sex differences in islet stress responses support female beta cell resilience. Mol Metab 2023;69:101678
23. Scrucca L, Fop M, Murphy TB, Raftery AE: mclust 5: Clustering, Classification and Density Estimation Using Gaussian Finite Mixture Models. R J 2016;8:289-317
24. Cui YF, Ma M, Wang GY, Han DE, Vollmar B, Menger MD: Prevention of core cell damage in isolated islets of Langerhans by low temperature preconditioning. World J Gastroenterol 2005;11:545-550
25. Jain C, Ansarullah, Bilekova S, Lickert H: Targeting pancreatic beta cells for diabetes treatment. Nat Metab 2022;4:1097-1108
26. Martens GA, Jiang L, Hellemans KH, Stange G, Heimberg H, Nielsen FC, Sand O, Van Helden J, Van Lommel L, Schuit F, Gorus FK, Pipeleers DG: Clusters of conserved beta cell marker genes for assessment of beta cell phenotype. PLoS One 2011;6:e24134
27. Mugabo Y, Zhao C, Tan JJ, Ghosh A, Campbell SA, Fadzeyeva E, Pare F, Pan SS, Galipeau M, Ast J, Broichhagen J, Hodson DJ, Mulvihill EE, Petropoulos S, Lim GE: 14-3-3zeta Constrains insulin secretion by regulating mitochondrial function in pancreatic beta cells. JCI Insight 2022;7
28. Cruciani-Guglielmacci C, Meneyrol K, Denom J, Kassis N, Rachdi L, Makaci F, Migrenne-Li S, Daubigney F, Georgiadou E, Denis RG, Rodriguez Sanchez-Archidona A, Paul JL, Thorens B, Rutter GA, Magnan C, Le Stunff H, Janel N: Homocysteine Metabolism Pathway Is Involved in the Control of Glucose Homeostasis: A Cystathionine Beta Synthase Deficiency Study in Mouse. Cells 2022;11
29. Laboute T, Zucca S, Holcomb M, Patil DN, Garza C, Wheatley BA, Roy RN, Forli S, Martemyanov KA: Orphan receptor GPR158 serves as a metabotropic glycine receptor: mGlyR. Science 2023;379:1352-1358
30. Yan-Do R, Duong E, Manning Fox JE, Dai X, Suzuki K, Khan S, Bautista A, Ferdaoussi M, Lyon J, Wu X, Cheley S, MacDonald PE, Braun M: A Glycine-Insulin Autocrine Feedback Loop Enhances Insulin Secretion From Human β-Cells and Is Impaired in Type 2 Diabetes. Diabetes 2016;65:2311-2321
31. Alam CM, Silvander JS, Daniel EN, Tao GZ, Kvarnstrom SM, Alam P, Omary MB, Hanninen A, Toivola DM: Keratin 8 modulates beta-cell stress responses and normoglycaemia. J Cell Sci 2013;126:5635-5644
32. Weidemann BJ, Marcheva B, Kobayashi M, Omura C, Newman MV, Kobayashi Y, Waldeck NJ, Perelis M, Lantier L, McGuinness OP, Ramsey KM, Stein RW, Bass J: Repression of latent NF-

kappaB enhancers by PDX1 regulates beta cell functional heterogeneity. Cell Metab 2024;36:90-102 e107
33. Pelligra A, Mrugala J, Griess K, Kirschner P, Nortmann O, Bartosinska B, Koster A, Krupenko NI, Gebel D, Westhoff P, Steckel B, Eberhard D, Herebian D, Belgardt BF, Schrader J, Weber APM, Krupenko SA, Lammert E: Pancreatic islet protection at the expense of secretory function involves serine-linked mitochondrial one-carbon metabolism. Cell Rep 2023;42:112703
34. Noordstra I, van den Berg CM, Boot FWJ, Katrukha EA, Yu KL, Tas RP, Portegies S, Viergever BJ, de Graaff E, Hoogenraad CC, de Koning EJP, Carlotti F, Kapitein LC, Akhmanova A: Organization and dynamics of the cortical complexes controlling insulin secretion in beta-cells. J Cell Sci 2022;135
35. Mziaut H, Mulligan B, Hoboth P, Otto O, Ivanova A, Herbig M, Schumann D, Hildebrandt T, Dehghany J, Sonmez A, Munster C, Meyer-Hermann M, Guck J, Kalaidzidis Y, Solimena M: The F-actin modifier villin regulates insulin granule dynamics and exocytosis downstream of islet cell autoantigen 512. Mol Metab 2016;5:656-668
36. Moss ND, Wells KL, Theis A, Kim YK, Spigelman AF, Liu X, MacDonald PE, Sussel L: Modulation of insulin secretion by RBFOX2-mediated alternative splicing. Nat Commun 2023;14:7732
37. Liu X, Yan F, Yao H, Chang M, Qin J, Li Y, Wang Y, Pei X: Involvement of RhoA/ROCK in insulin secretion of pancreatic beta-cells in 3D culture. Cell Tissue Res 2014;358:359-369
38. Johnson JD, Bernal-Mizrachi E, Alejandro EU, Han Z, Kalynyak TB, Li H, Beith JL, Gross J, Warnock GL, Townsend RR, Permutt MA, Polonsky KS: Insulin protects islets from apoptosis via Pdx1 and specific changes in the human islet proteome. Proc Natl Acad Sci U S A 2006;103:19575-19580
39. Loughlin FE, Mansfield RE, Vaz PM, McGrath AP, Setiyaputra S, Gamsjaeger R, Chen ES, Morris BJ, Guss JM, Mackay JP: The zinc fingers of the SR-like protein ZRANB2 are single-stranded RNA-binding domains that recognize 5' splice site-like sequences. Proc Natl Acad Sci U S A 2009;106:5581-5586
40. Colwill K, Feng LL, Yeakley JM, Gish GD, Caceres JF, Pawson T, Fu XD: SRPK1 and Clk/Sty protein kinases show distinct substrate specificities for serine/arginine-rich splicing factors. J Biol Chem 1996;271:24569-24575
41. Thuresson AC, Astrom J, Astrom A, Gronvik KO, Virtanen A: Multiple forms of poly(A) polymerases in human cells. Proc Natl Acad Sci U S A 1994;91:979-983
42. Wiegard A, Kuzin V, Cameron DP, Grosser J, Ceribelli M, Mehmood R, Ballarino R, Valant F, Grochowski R, Karabogdan I, Crosetto N, Lindqvist A, Bizard AH, Kouzine F, Natsume T, Baranello L: Topoisomerase 1 activity during mitotic transcription favors the transition from mitosis to G1. Mol Cell 2021;81:5007-5024 e5009
43. Bacon CW, D'Orso I: CDK9: a signaling hub for transcriptional control. Transcription 2019;10:57-75
44. Liu X, Bushnell DA, Kornberg RD: RNA polymerase II transcription: structure and mechanism. Biochim Biophys Acta 2013;1829:2-8
45. Fukuda A, Nogi Y, Hisatake K: The regulatory role for the ERCC3 helicase of general transcription factor TFIIH during promoter escape in transcriptional activation. Proc Natl Acad Sci U S A 2002;99:1206-1211
46. Gallinari P, Di Marco S, Jones P, Pallaoro M, Steinkuhler C: HDACs, histone deacetylation and gene transcription: from molecular biology to cancer therapeutics. Cell Res 2007;17:195-211
47. O'Connor L, Gilmour J, Bonifer C: The Role of the Ubiquitously Expressed Transcription Factor Sp1 in Tissue-specific Transcriptional Regulation and in Disease. Yale J Biol Med 2016;89:513-525
48. Chen Y, Brandizzi F: IRE1: ER stress sensor and cell fate executor. Trends Cell Biol 2013;23:547-555
49. Johnston NR, Mitchell RK, Haythorne E, Pessoa MP, Semplici F, Ferrer J, Piemonti L, Marchetti P, Bugliani M, Bosco D, Berishvili E, Duncanson P, Watkinson M, Broichhagen J, Trauner D, Rutter GA, Hodson DJ: Beta Cell Hubs Dictate Pancreatic Islet Responses to Glucose. Cell Metab 2016;24:389-401

50. Kim A, Miller K, Jo J, Kilimnik G, Wojcik P, Hara M: Islet architecture: A comparative study. Islets 2009;1:129-136
51. Chabosseau P, Yong F, Delgadillo-Silva LF, Lee EY, Melhem R, Li S, Gandhi N, Wastin J, Noriega LL, Leclerc I, Ali Y, Hughes JW, Sladek R, Martinez-Sanchez A, Rutter GA: Molecular phenotyping of single pancreatic islet leader beta cells by "Flash-Seq". Life Sci 2023;316:121436
52. Neukam M, Sala P, Brunner AD, Ganss K, Palladini A, Grzybek M, Topcheva O, Vasiljevic J, Broichhagen J, Johnsson K, Kurth T, Mann M, Coskun U, Solimena M: Purification of time-resolved insulin granules reveals proteomic and lipidomic changes during granule aging. Cell Rep 2024;43:113836
53. Dror E, Fagnocchi L, Wegert V, Apostle S, Grimaldi B, Gruber T, Panzeri I, Heyne S, Hoffler KD, Kreiner V, Ching R, Tsai-Hsiu Lu T, Semwal A, Johnson B, Senapati P, Lempradl A, Schones D, Imhof A, Shen H, Pospisilik JA: Epigenetic dosage identifies two major and functionally distinct beta cell subtypes. Cell Metab 2023;35:821-836 e827
54. Yu V, Yong F, Marta A, Khadayate S, Osakwe A, Bhattacharya S, Varghese SS, Chabosseau P, Tabibi SM, Chen K, Georgiadou E, Parveen N, Suleiman M, Stamoulis Z, Marselli L, De Luca C, Tesi M, Ostinelli G, Delgadillo-Silva L, Wu X, Hatanaka Y, Montoya A, Elliott J, Patel B, Demchenko N, Whilding C, Hajkova P, Shliaha P, Kramer H, Ali Y, Marchetti P, Sladek R, Dhawan S, Withers DJ, Rutter GA, Millership SJ: Differential CpG methylation at Nnat in the early establishment of beta cell heterogeneity. Diabetologia 2024;67:1079-1094
55. Oetjen E, Baun D, Beimesche S, Krause D, Cierny I, Blume R, Dickel C, Wehner S, Knepel W: Inhibition of human insulin gene transcription by the immunosuppressive drugs cyclosporin A and tacrolimus in primary, mature islets of transgenic mice. Mol Pharmacol 2003;63:1289-1295
56. Lawrence MC, Bhatt HS, Easom RA: NFAT regulates insulin gene promoter activity in response to synergistic pathways induced by glucose and glucagon-like peptide-1. Diabetes 2002;51:691-698
57. Soleimanpour SA, Crutchlow MF, Ferrari AM, Raum JC, Groff DN, Rankin MM, Liu C, De Leon DD, Naji A, Kushner JA, Stoffers DA: Calcineurin signaling regulates human islet beta-cell survival. J Biol Chem 2010;285:40050-40059
58. Tengholm A, Gylfe E: cAMP signalling in insulin and glucagon secretion. Diabetes Obes Metab 2017;19 Suppl 1:42-53
59. Han P, Werber J, Surana M, Fleischer N, Michaeli T: The calcium/calmodulin-dependent phosphodiesterase PDE1C down-regulates glucose-induced insulin secretion. J Biol Chem 1999;274:22337-22344
60. Pratt EPS, Harvey KE, Salyer AE, Hockerman GH: Regulation of cAMP accumulation and activity by distinct phosphodiesterase subtypes in INS-1 cells and human pancreatic beta-cells. PLoS One 2019;14:e0215188
61. Shibata H, Robinson FW, Soderling TR, Kono T: Effects of okadaic acid on insulin-sensitive cAMP phosphodiesterase in rat adipocytes. Evidence that insulin may stimulate the enzyme by phosphorylation. J Biol Chem 1991;266:17948-17953
62. Tang X, Wang C, Hsieh Y, Wang C, Wang J, Han Z, Cong N, Ma R, Chi F: Triptolide induces toxicity in inner ear stem cells via promoting DNA damage. Toxicol In Vitro 2019;61:104597
63. Ergin M, Dundar ZD, Kilinc I, Colak T, Oltulu P, Girisgin AS: Alpha-Amanitin Poisoning, Nephrotoxicity and Oxidative Stress: An Experimental Mouse Model. Iran Red Crescent Med J 2015;17:e28068
64. Tang D, Lahti JM, Grenet J, Kidd VJ: Cycloheximide-induced T-cell death is mediated by a Fas-associated death domain-dependent mechanism. J Biol Chem 1999;274:7245-7252
65. Borowczak J, Szczerbowski K, Ahmadi N, Szylberg L: CDK9 inhibitors in multiple myeloma: a review of progress and perspectives. Med Oncol 2022;39:39
66. Su H, Peng C, Liu Y: Regulation of ferroptosis by PI3K/Akt signaling pathway: a promising therapeutic axis in cancer. Front Cell Dev Biol 2024;12:1372330
67. Bryanskaya EO, Vinokurov AY, Dolgikh AI, Dunaev AV, Angelova PR, Abramov AY: High levels of FAD autofluorescence indicate pathology preceding cell death. Biochim Biophys Acta Gen Subj 2024;1868:130520

68. Kwon G, Pappan KL, Marshall CA, Schaffer JE, McDaniel ML: cAMP Dose-dependently prevents palmitate-induced apoptosis by both protein kinase A- and cAMP-guanine nucleotide exchange factor-dependent pathways in beta-cells. J Biol Chem 2004;279:8938-8945
69. Yusta B, Baggio LL, Estall JL, Koehler JA, Holland DP, Li H, Pipeleers D, Ling Z, Drucker DJ: GLP-1 receptor activation improves beta cell function and survival following induction of endoplasmic reticulum stress. Cell Metab 2006;4:391-406

Author Contributions:
CM. J. C. designed studies, performed experiments, analyzed/interpreted data, wrote manuscript.
B. S. performed experiments, analyzed/interpreted data, wrote parts of manuscript.
H. H. C. analyzed/interpreted data.
X. H. performed experiments.
W. G. S. performed experiments.
G. P. B. performed experiments and analyzed/interpreted data.
Y. H. X. analyzed/interpreted data.
J. R. performed experiments, analyzed/interpreted data, wrote parts of manuscript.
J. D. J. conceived the project, designed studies, interpreted data, and edited the manuscript.

Declaration of Interests: The authors declare no competing interests.

Funding: Research was supported by a CIHR operating grant (PJT152999) to J.D.J., the JDRF Centre of Excellence at UBC, and core facilities in the Life Sciences Institute.

Acknowledgments: We thank many colleagues for helpful discussions during conferences, meetings, and presentations.

Guarantors: J.D.J. is the guarantor of this work and, as such, had full access to all the data in the study and takes responsibility for the integrity of the data and the accuracy of the data analysis.

Data Resource Sharing and Availability: Proteomic data are available on ProteomExchange (number PXD052023).

Table 1. Key resources

Reagent/resource	Designation	Source/reference	RRID
Ins2^{GFP} knock-in mouse model	Mouse model	Wakae-takada et al., 2013(14)	N/A
Chemical compound	Collagenase P	Sigma, catalog number C7657	N/A
Reagent	RPMI 1640	Invitrogen, catalog number 11875	N/A
Reagent	Fetal bovine serum	Invitrogen, catalog number 12483020	N/A
Software	GraphPad Prism	GraphPad Software	N/A
Software	ImageXpress	Molecular Devices	N/A
Software	R	R Foundation for Statistical Computing	N/A

Table 2. Reagents used in the small molecule screen

Drug	Concentration	Vendor	Catalogue #	Reference PMID
Cyclohexamide	355 μM	Sigma Aldrich	C7698	32844746
Sal003	5 μM	Sigma Aldrich	S4451	28009255
CCT020312	0.2 μM	Calbiochem	324879	28148553
DHBDC	20 μM	Calbiochem	5315510001	23784735
ISRIB	0.2 μM	Sigma Aldrich	SML0843	25858979
GSK2606414 / Perk inhibitor 1	0.03 μM	Sigma Aldrich	516535	22827572
PKRi/C16	2 μM	Sigma Aldrich	I9785	31723021
Thapsigargin	1 μM	Millipore	586005	36690328
Tunicamycin	0.1 μM	Sigma Aldrich	T7765	32268491
Eeyarestatin I	10 μM	Sigma Aldrich	E1286	21124757
APY 29	20 μM	Sigma Aldrich	SML2381	25018104
Sunitinib	5 μM	Sigma Aldrich	PZ0012	28449948
Azoramide	20 μM	Sigma Aldrich	SML1560	26084805
Tacrolimus / FK506	0.03 μM	Selleck Chem	S5003	12761338
Cylcosporin A	5 μM	Selleck Chem	S2286	12761338
LY 294002	50 μM	Sigma Aldrich	L9908	18202127

Wortmannin	0.1 μM	Sigma Aldrich	W1628	8666133
Sodium butyrate	1000 μM	Sigma Aldrich	B5887	2843409
Trichostatin A (TSA)	0.625 μM	Sigma Aldrich	T1952	25305500
MGCD0103/Mocetinostat	25 μM	Selleck Chem	S1122	18413790
Somatostatin (SST)	1 μM	Sigma Aldrich	S9129	7907998
Epinephrine	50 μM	Sigma Aldrich	E4250	7907998
GLP-1 amide	0.01 μM	R&D systems	2082	10909973
Rosiglitazone	10 μM	Sigma Aldrich	R2408	19338578
Staurosporine	0.1 μM	Sigma Aldrich	S4400	14510500
Okadaic	0.1 μM	Sigma Aldrich	O9381	8183910
Palmitate	0.5 μM	Sigma Aldrich	P9767	15944145
Metformin	0.5 μM	Sigma Aldrich	PHR1084	27662780
Dexamethasone (DEX)	0.1 μM	Sigma Aldrich	D4902	28406939
Isoxazole 9 (ISX-9)	40 μM	Selleck Chem	S7914	22143803
AS1842856	1 μM	Calbiochem	344355	25483084
Diazoxide	100 μM	Sigma Aldrich	D9035	17229937
IBMX	100 μM	Sigma Aldrich	I5879	6201163
Arginine	10000 μM	Sigma Aldrich	A8094	25205820
Verapamil	2.7 μM	Sigma Aldrich	V4629	1095438
Ryanodine	10 μM	Millipore	559276	15033925
5-amino-imidazole carboxamide riboside (AICAR)	300 μM	Sigma Aldrich	A9978	15823553
Pramlintide	1 μM	Sigma Aldrich	SML2523	1311671
Tolbutamide	0.37 μM	Sigma Aldrich	T0891	6988275
HNMPA	100 μM	Abcam	ab141566	18202127
S961	0.1 μM	Phoenix Peptide	051-86	26740601
Bortezomib	0.004 μM	Sigma Aldrich	5043140001	19190324
MG132	0.4 μM	Sigma Aldrich	M8699	19190324
xestospongin C	2 μM	Sigma Aldrich	X2628	23302634
Actinomycin D	2 μM	Sigma Aldrich	A9415	21922053
α-amanitin	2 μM	Sigma Aldrich	A2263	24213132
Triptolide	0.1 μM	Sigma Aldrich	T3652	24213132
5,6-Dichloro-1-beta-Ribo-furanosyl Benzimidazole (DRB)	50 μM	Sigma Aldrich	D1916	24213132

Figure Legends

Figure 1. Live 3D imaging of intact *Ins2*^{GFP} mouse islets. (A) Schematic of the *Ins2*^{GFP} knock-in mouse model, in which the second exon of the wildtype *Ins2* gene has been partially replaced with GFP. **(B)** FACS purification of *Ins2*(GFP)^{LOW} and *Ins2*(GFP)^{HIGH} populations of β cells, with β cells isolated from a WT mouse for comparison. **(C)** Example images of 3D live cell imaging of intact islets from *Ins2*^{GFP} knock-in mice. Hoechst is a cell nuclei dye. Scale bar is 30 µm. **(D)** Distribution of cells based on GFP fluorescence from *Ins2*^{GFP} islets. Each distribution line represents an islet. (n = 40 islets). **(E)** Comparison of ratios of high GFP cells to low GFP cells in male and female mice. Each dot represents an islet (n = 20 male and 20 female islets from 3 male and 3 female mice). **(F)** Nearest neighbor analysis of cells from *Ins2*^{GFP} knock-in mice (n = 40 islets). One-way ANOVA. **(G)** Distance to core of cells from *Ins2*^{GFP} knock-in mice. Student's T-test. Density: probability density function, represents the probability a data is located within the defined range (i.e. ratio of the total). Error bars are SEM. * $p < 0.05$

Figure 2. Proteomic analysis of FACS purified *Ins2*^{GFP} β cells. (A) Volcano plot of differentially expressed proteins comparing FACS purified GFP positive and GFP negative cells. **(B)** Volcano plot of differentially expressed proteins comparing FACS purified *Ins2*(GFP)^{HIGH} and *Ins2*(GFP)^{LOW} cells. **(C)** Gene set enrichment analysis of pathways enriched in GFP positive and GFP negative cells. **(D)** Gene set enrichment analysis of pathways enriched in *Ins2*(GFP)^{HIGH} and *Ins2*(GFP)^{LOW} cells.

Figure 3. Integration of STRING networks and protein expression data in Cytoscape reveals differences in protein production and export between GFP positive and GFP negative cells. (A) Integration of STRING networks and protein expression data of differentially abundant proteins (top 100 with p value lower than 0.05) in GFP negative cells in Cytoscape. Deeper color of the nodes represents the fold change (GFP negative/GFP negative), while the thickness of the line around the node represents p value. **(B)** Integration of STRING networks and protein expression data of differentially abundant proteins (top 100 with p value lower than 0.05) in GFP positive cells in Cytoscape. Deeper color of the nodes represents the fold change (GFP positive/GFP negative), while the thickness of the line around the node represents p value.

Figure 4. Integration of STRING networks and protein expression data in Cytoscape reveals differences in transcription and mRNA processing between GFP expression states. (A) Integration of STRING networks and protein expression data of differentially abundant proteins (p value lower than 0.05) in *Ins2*(GFP)^{HIGH} cells in Cytoscape. Deeper color of the nodes represents the fold change (*Ins2*(GFP)^{LOW}/*Ins2*(GFP)^{HIGH}), while the thickness of the line around the node represents p value **(B)** Integration of STRING networks and protein expression data of differentially abundant proteins (p value lower than 0.05) in *Ins2*(GFP)^{LOW} cells in Cytoscape. Deeper color of the nodes represents the fold change (*Ins2*(GFP)^{HIGH}/*Ins2*(GFP)^{LOW}), while the thickness of the line around the node represents p value.

Figure 5. OPP protein synthesis assay of *Ins2*(GFP)^{LOW} and *Ins2*(GFP)^{HIGH} cells. (A) Representative images of OPP protein synthesis assay on *Ins2*$^{WT/GFP}$ mice. The blue wavelength is

the Nuclearmask cell nuclei stain, the green wavelength is GFP, and the red wavelength is the OPP marker for nascent peptide formation. Scale bar is 40 µm. **(B)** Comparison of translational capacity of GFP positive β cells and GFP negative cells (n = 6 mice). Student's t-test. **(C)** Comparison of translational capacity of *Ins2*(GFP)^{HIGH} and *Ins2*(GFP)^{LOW} cells (n = 6 mice). Student's t-test. **(D)** GFP fluorescence of *Ins2*(GFP)^{LOW} β cells and *Ins2*(GFP)^{HIGH} β cells. Student's t-test (n=6 mice). Error bars are SEM.

Figure 6. A small molecule screen for effectors of *Ins2* gene activity. (A) Experiment pipeline. Islets were isolated and dispersed from *Ins2*^{GFP} knock-in mice. Cells were then stained with Hoechst cell nuclei dye and propidium iodide (PI) cell death marker for two hours, then subjected to treatments. Live cell imaging was then performed, and fluorescence for all three wavelengths was tracked across 96 hours of imaging. **(B-L)** Average GFP fluorescence of cells over the period of 96 hours. Each line represents a treatment. Treatments were categorized based on their primary binding partners. Deceased cells were removed by thresholding for cells with high PI fluorescence. Dotted black lines indicate DMSO controls, dashed lines indicate inhibitors of their respective categories, and solid lines indicate activators of their respective categories (n = 6 mice). Shading represents SEM. **(M)** Analysis of GFP fluorescence against cell death. GFP fluorescence is scaled GFP fluorescence relative to background after 48 hours of treatment. Cell death is scaled PI fluorescence relative to background after 72 hours of treatment. Size of dots represents p value (adjusted). Colors of dots represents categories, which were decided based on their primary binding partners (n = 6 mice). Two-way ANOVA, adjusted p value indicated by size of dots.

Figure 7. Cell state transitions in the context of various media conditions and perturbations. (A) Transition rates between the *Ins2(*GFP)^{HIGH} and *Ins2(*GFP)^{LOW} cell states in the context of various media conditions. % of cells transitioning: percent of subpopulation transitioning to other cell state after 48 hours of culture. **(B)** Example images of increasing GFP fluorescence in response to IBMX. **(C)** Example traces of GFP upregulation and cell state transitions in response to IBMX and GLP-1 amide. **(D)** Comparison of *Ins2(*GFP)^{HIGH} to *Ins2(*GFP)^{LOW} and *Ins2(*GFP)^{LOW} to *Ins2(*GFP)^{HIGH} transition rates in the context of the small molecule screen. Data shown is average transition rate by the end of 48 hours of treatment (n = 6 mice). Size of the dots denotes p value (adjusted). Color of the dots denotes scaled GFP fluorescence. Two-way ANOVA.

Figure 8. Integration of STRING protein networks and a small molecule screen on Cytoscape. (A) Primary binding partners for small molecules used in the screen localized in Cytoscape. Binding partners (bold) are chosen based on their affinity to the small molecule. Color of the nodes represents GFP fluorescence (scaled) after 48 hours of treatment. Borders of the nodes represents cell death (scaled PI fluorescence) after 72 hours of treatment. Height of green triangles represents *Ins2(*GFP)^{LOW} to *Ins2(*GFP)^{HIGH} transition rates. Height of orange triangles represents *Ins2(*GFP)^{HIGH} to *Ins2(*GFP)^{LOW} transition rates. Blue lines represent STRING interactions. Pointed arrows with grey lines represents upregulation. Inhibitor arrows with grey lines represents downregulation.

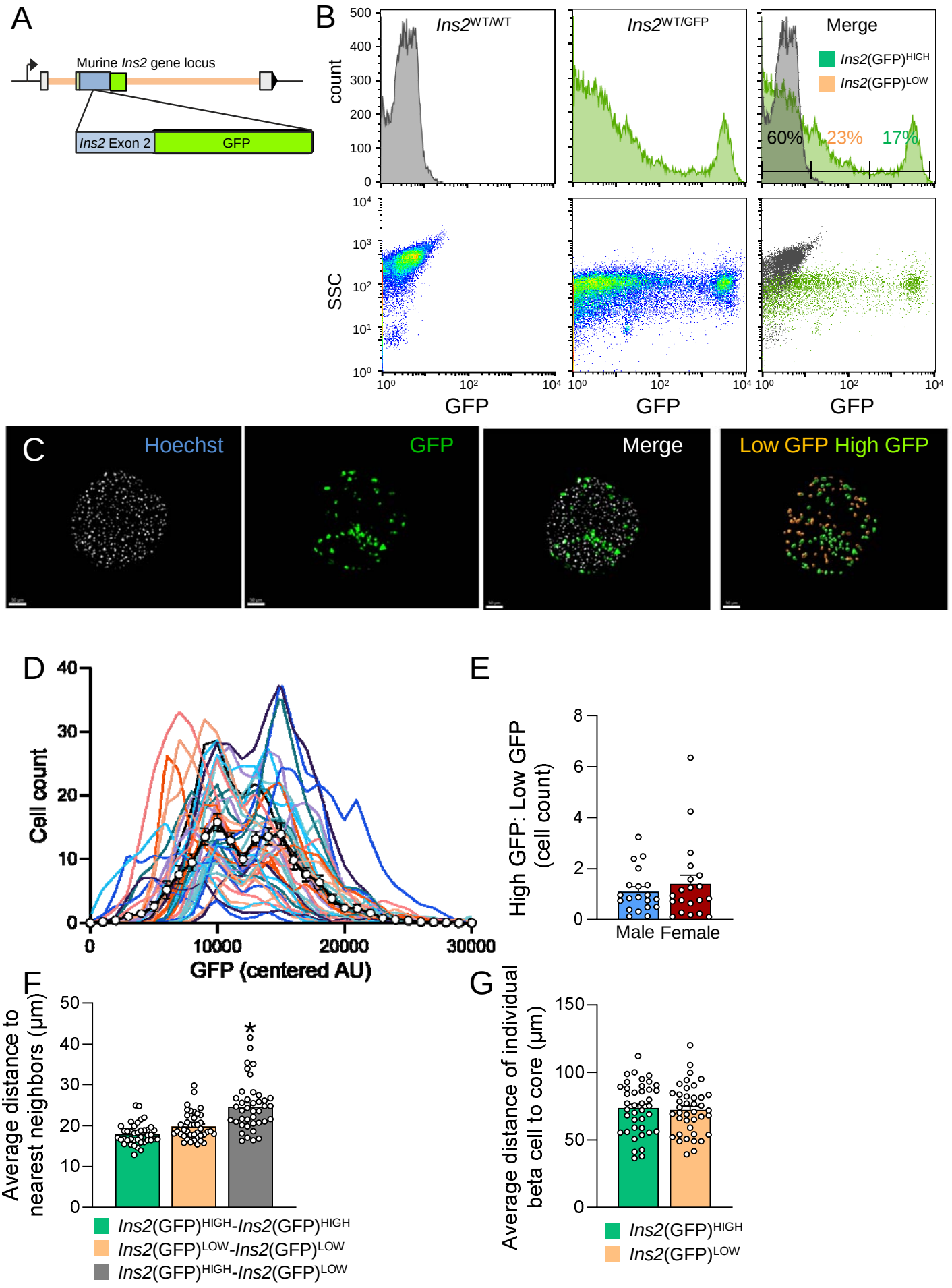
A
Murine Ins2 gene locus
Ins2 Exon 2
GFP
B
Ins2WT/WT
Ins2WT/GFP
Merge
Ins2(GFP)HIGH
Ins2(GFP)LOW
60%
23%
17%
count
SSC
GFP
C
Hoechst
GFP
Merge
Low GFP High GFP
D
Cell count
GFP (centered AU)
E
High GFP: Low GFP (cell count)
Male
Female
F
Average distance to nearest neighbors (µm)
Ins2(GFP)HIGH-Ins2(GFP)HIGH
Ins2(GFP)LOW-Ins2(GFP)LOW
Ins2(GFP)HIGH-Ins2(GFP)LOW
G
Average distance of individual beta cell to core (µm)
Ins2(GFP)HIGH
Ins2(GFP)LOW

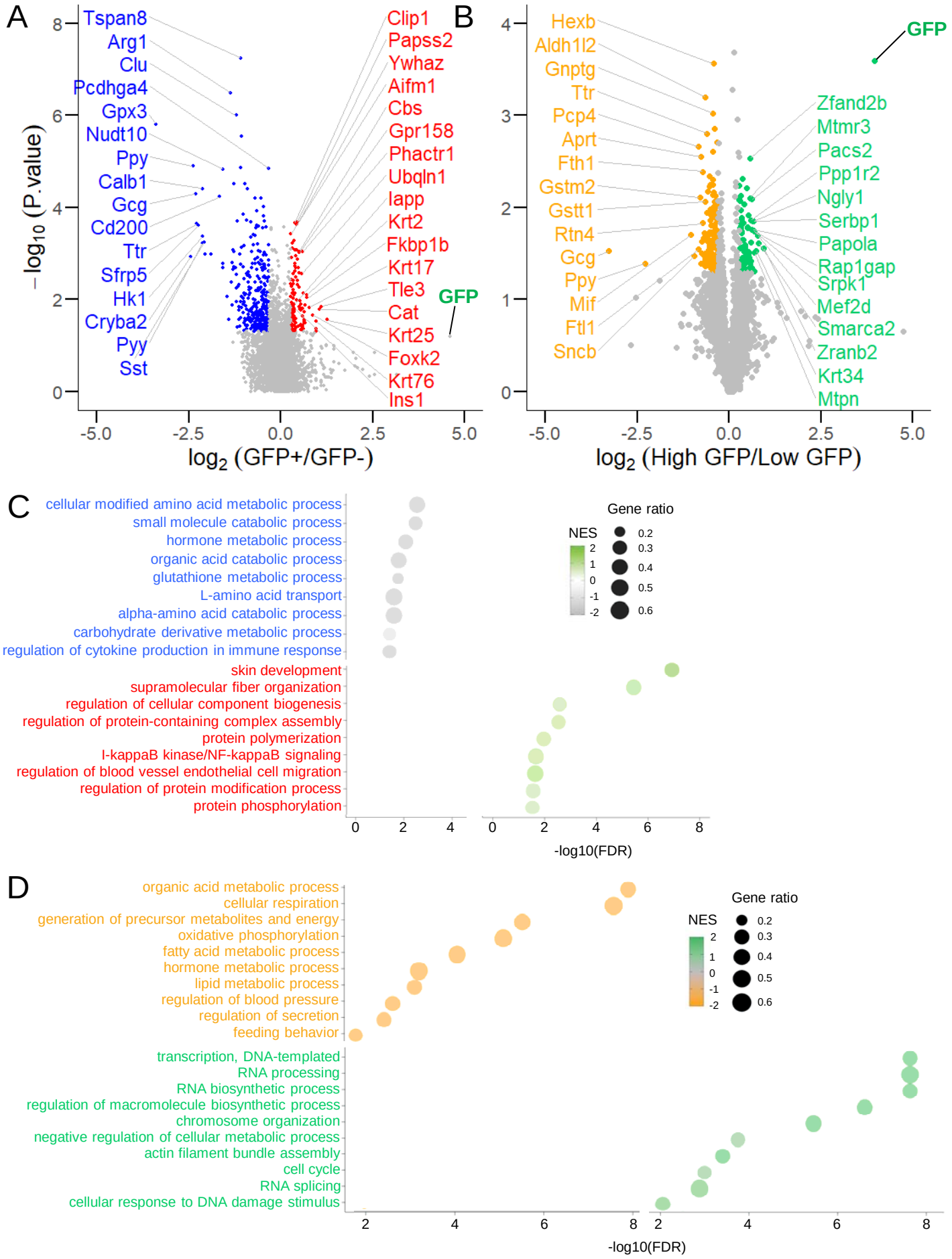
A
Tspan8
Arg1
Clu
Pcdhga4
Gpx3
Nudt10
Ppy
Calb1
Gcg
Cd200
Ttr
Sfrp5
Hk1
Cryba2
Pyy
Sst
Clip1
Papss2
Ywhaz
Aifm1
Cbs
Gpr158
Phactr1
Ubqln1
Iapp
Krt2
Fkbp1b
Krt17
Tle3
Cat
Krt25
Foxk2
Krt76
Ins1
GFP
−log10 (P.value)
log2 (GFP+/GFP-)
B
Hexb
Aldh1l2
Gnptg
Ttr
Pcp4
Aprt
Fth1
Gstm2
Gstt1
Rtn4
Gcg
Ppy
Mif
Ftl1
Sncb
GFP
Zfand2b
Mtmr3
Pacs2
Ppp1r2
Ngly1
Serbp1
Papola
Rap1gap
Srpk1
Mef2d
Smarca2
Zranb2
Krt34
Mtpn
log2 (High GFP/Low GFP)
C
cellular modified amino acid metabolic process
small molecule catabolic process
hormone metabolic process
organic acid catabolic process
glutathione metabolic process
L-amino acid transport
alpha-amino acid catabolic process
carbohydrate derivative metabolic process
regulation of cytokine production in immune response
skin development
supramolecular fiber organization
regulation of cellular component biogenesis
regulation of protein-containing complex assembly
protein polymerization
I-kappaB kinase/NF-kappaB signaling
regulation of blood vessel endothelial cell migration
regulation of protein modification process
protein phosphorylation
Gene ratio
NES
-log10(FDR)
D
organic acid metabolic process
cellular respiration
generation of precursor metabolites and energy
oxidative phosphorylation
fatty acid metabolic process
hormone metabolic process
lipid metabolic process
regulation of blood pressure
regulation of secretion
feeding behavior
transcription, DNA-templated
RNA processing
RNA biosynthetic process
regulation of macromolecule biosynthetic process
chromosome organization
negative regulation of cellular metabolic process
actin filament bundle assembly
cell cycle
RNA splicing
cellular response to DNA damage stimulus
Gene ratio
NES
-log10(FDR)

A

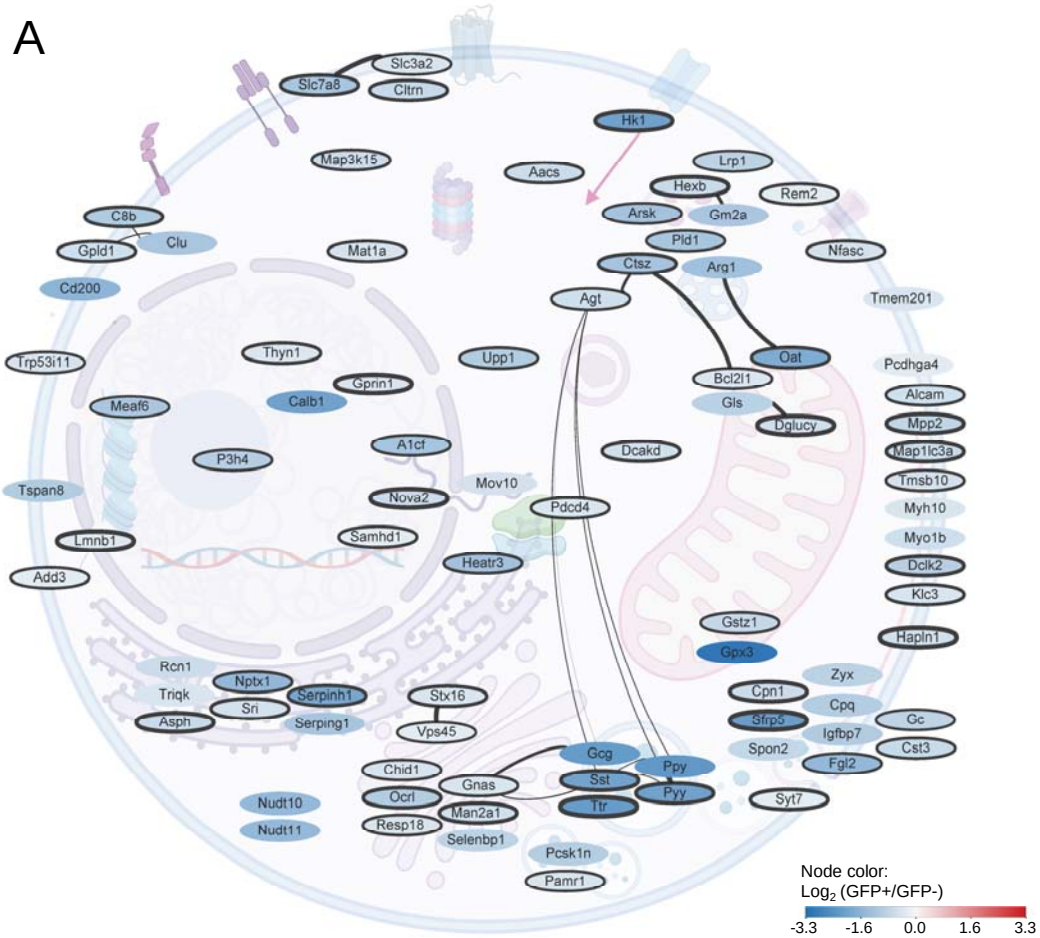
Slc3a2
Slc7a8
Cltrn
Hk1
Map3k15
Aacs
Lrp1
Hexb
Rem2
Arsk
Gm2a
C8b
Clu
Gpld1
Mat1a
Pld1
Nfasc
Ctsz
Arg1
Cd200
Agt
Tmem201
Trp53i11
Thyn1
Upp1
Oat
Pcdhga4
Gprin1
Bcl2l1
Meaf6
Calb1
Gls
Alcam
Dglucy
Mpp2
A1cf
Dcakd
Map1lc3a
P3h4
Tmsb10
Tspan8
Mov10
Nova2
Pdcd4
Myh10
Myo1b
Lmnb1
Samhd1
Dclk2
Add3
Heatr3
Klc3
Gstz1
Hapln1
Gpx3
Rcn1
Zyx
Nptx1
Triqk
Serpinh1
Stx16
Cpn1
Cpq
Sri
Sfrp5
Gc
Asph
Serping1
Vps45
Igfbp7
Spon2
Cst3
Gcg
Ppy
Chid1
Fgl2
Gnas
Sst
Ocrl
Pyy
Syt7
Nudt10
Ttr
Man2a1
Nudt11
Resp18
Selenbp1
Pcsk1n
Pamr1
Node color:
Log2 (GFP+/GFP-)
-3.3
-1.6
0.0
1.6
3.3
Node border thickness :
-Log10 (p-value)
42
1
1.3
1.9
2.5
3.1
3.7

B

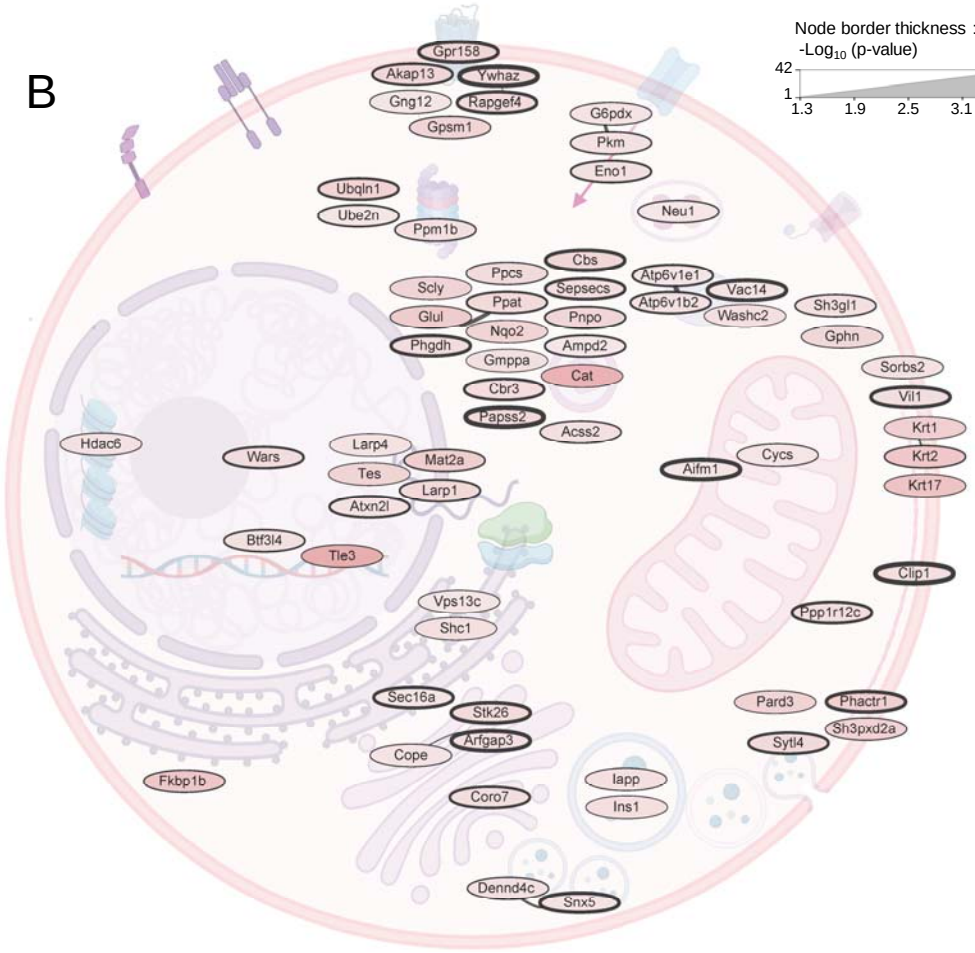
Gpr158
Akap13
Ywhaz
Gng12
Rapgef4
Gpsm1
G6pdx
Pkm
Eno1
Ubqln1
Ube2n
Ppm1b
Neu1
Cbs
Ppcs
Atp6v1e1
Scly
Sepsecs
Vac14
Atp6v1b2
Sh3gl1
Glul
Ppat
Washc2
Pnpo
Nqo2
Gphn
Phgdh
Ampd2
Gmppa
Sorbs2
Cat
Cbr3
Vil1
Papss2
Acss2
Krt1
Hdac6
Larp4
Wars
Mat2a
Cycs
Tes
Aifm1
Krt2
Larp1
Krt17
Atxn2l
Btf3l4
Tle3
Clip1
Vps13c
Ppp1r12c
Shc1
Sec16a
Pard3
Phactr1
Stk26
Sh3pxd2a
Arfgap3
Sytl4
Cope
Fkbp1b
Iapp
Coro7
Ins1
Dennd4c
Snx5

A

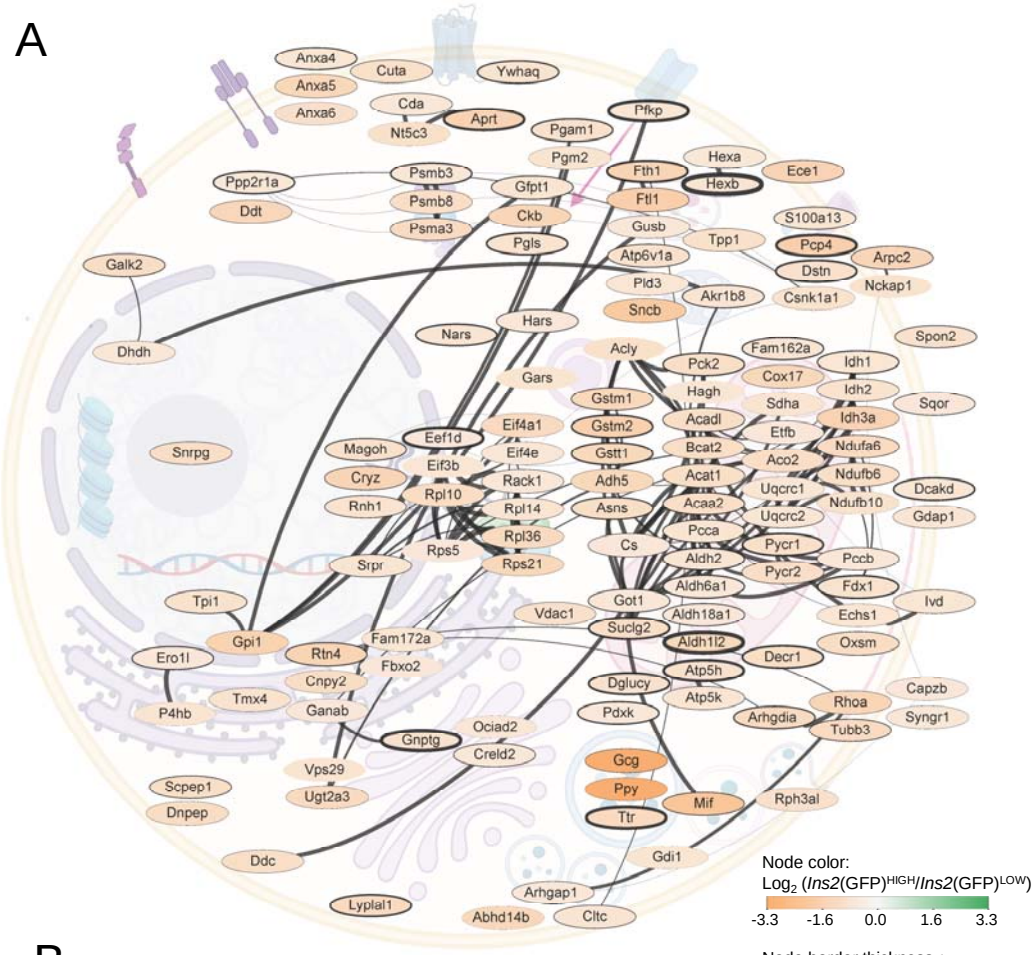

Node color:
Log_2 (*Ins2*(GFP)^{HIGH}/*Ins2*(GFP)^{LOW})

-3.3 -1.6 0.0 1.6 3.3

B

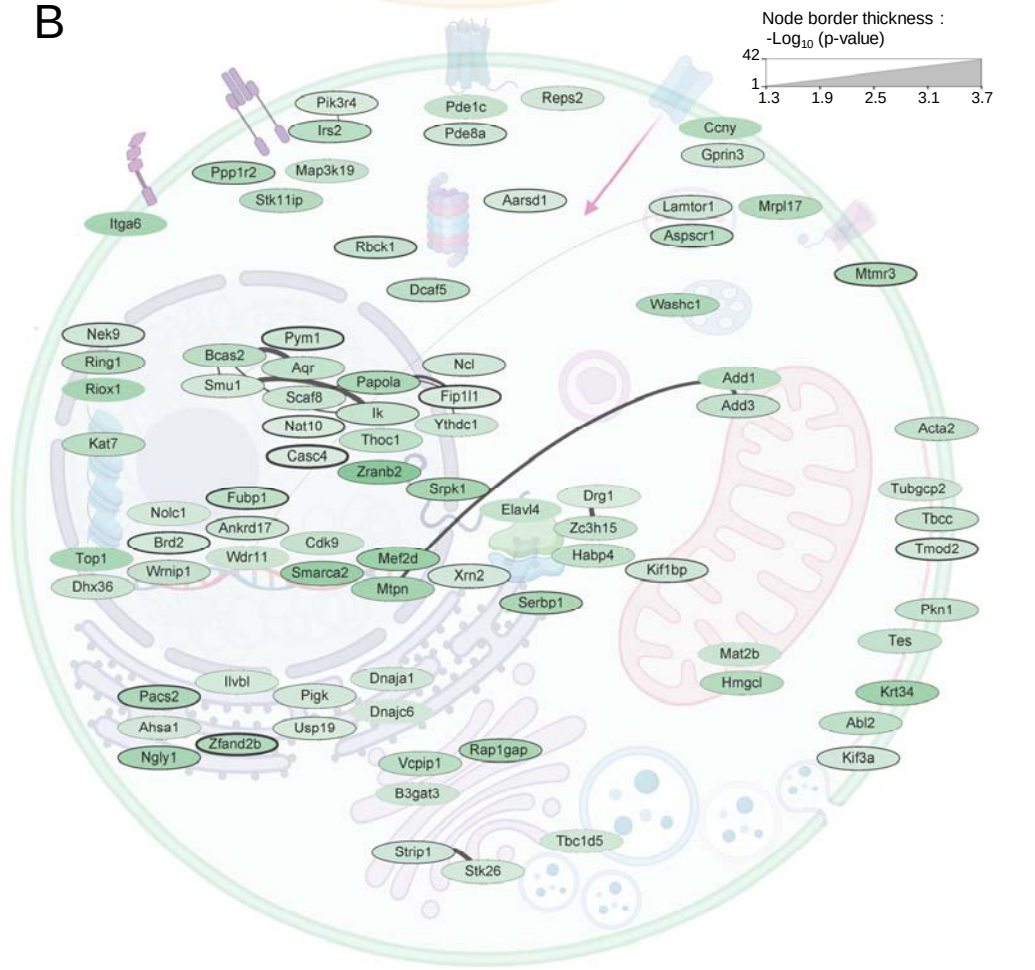

Node border thickness :
$-\text{Log}_{10}$ (p-value)

42
1
1.3 1.9 2.5 3.1 3.7

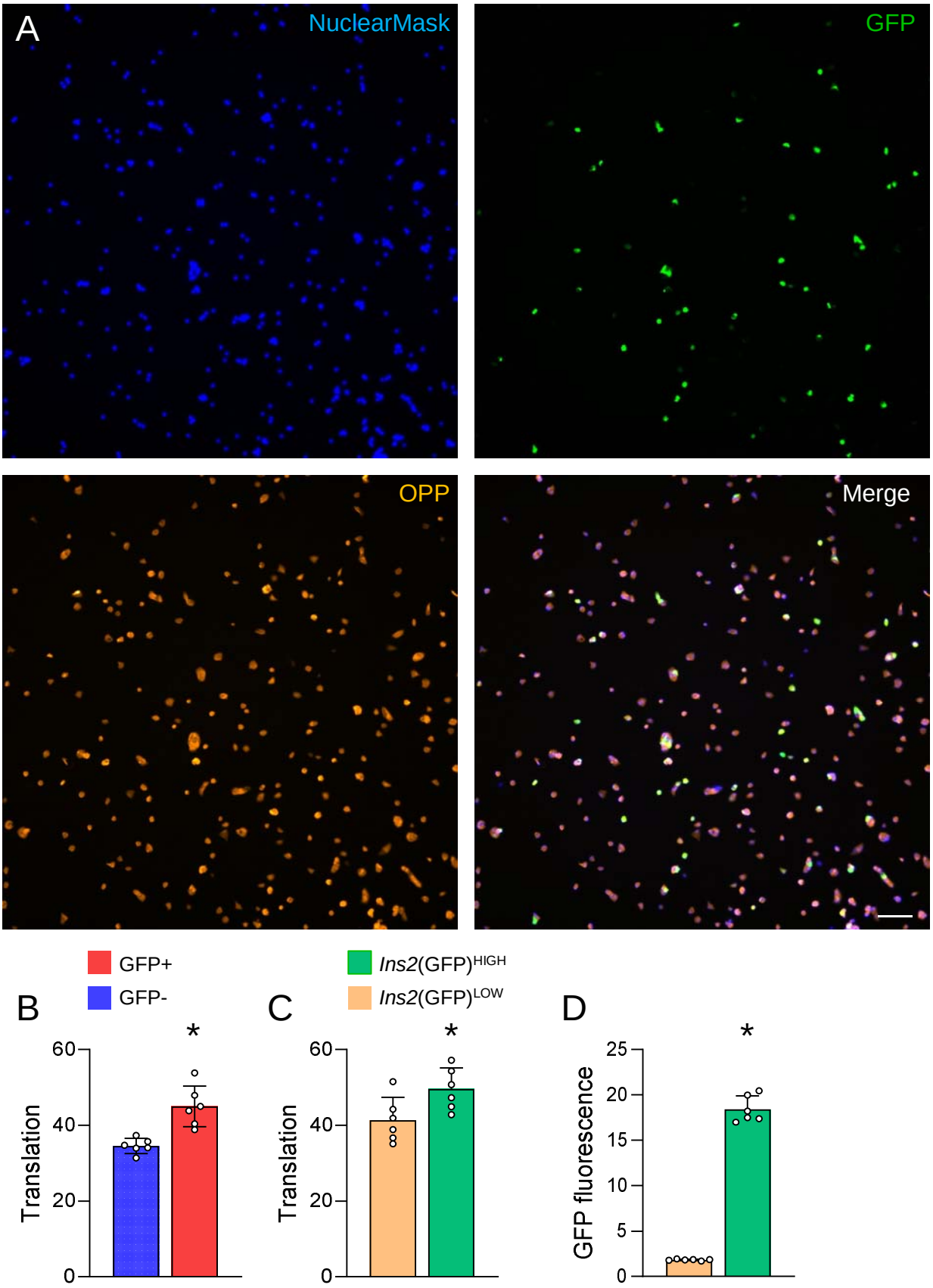
A
NuclearMask
GFP
OPP
Merge
GFP+
GFP-
B
Translation
60
40
20
0
*
Ins2(GFP)HIGH
Ins2(GFP)LOW
C
Translation
60
40
20
0
*
D
GFP fluorescence
25
20
15
10
5
0
*

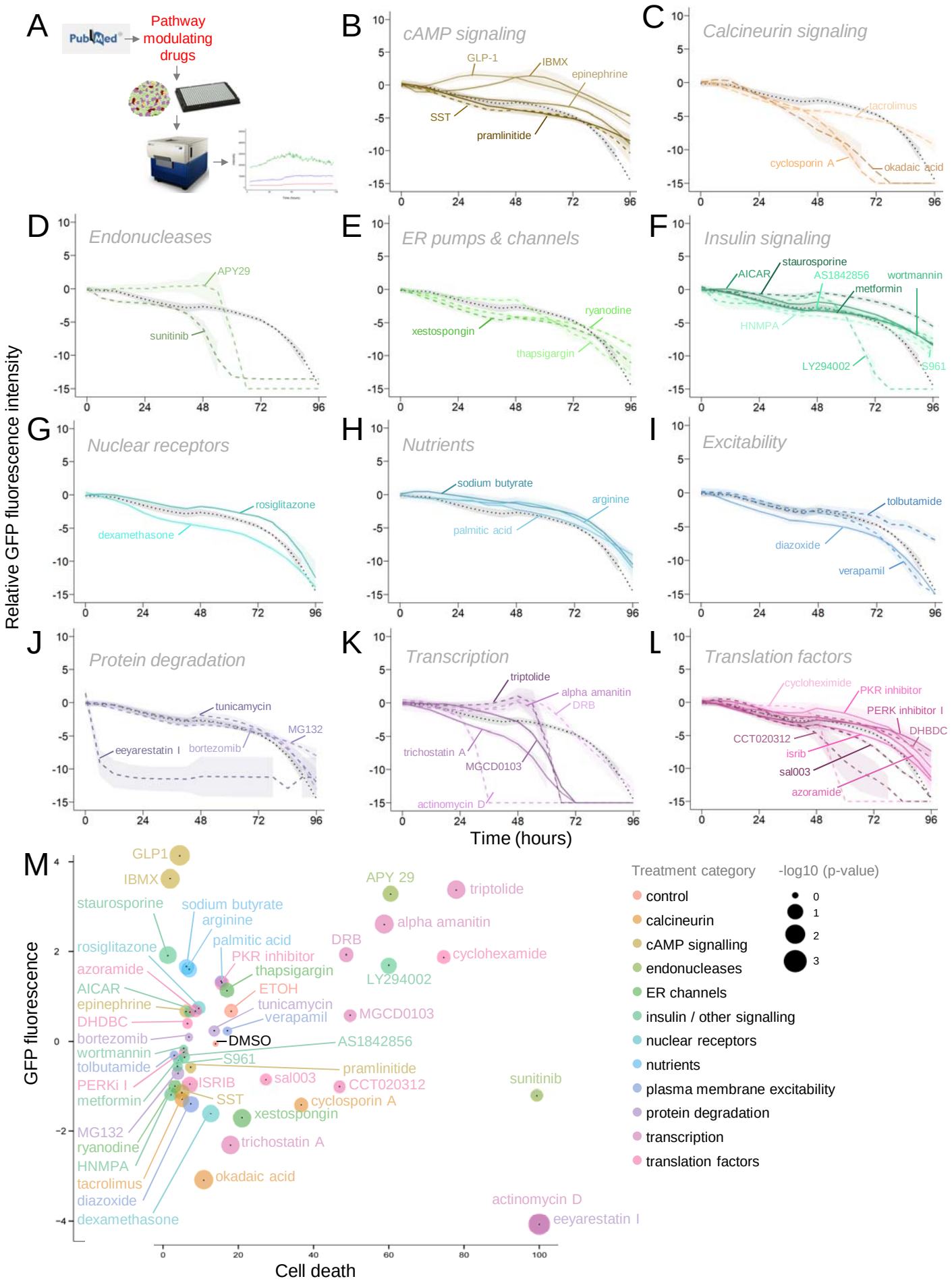
A
PubMed
Pathway modulating drugs
B
cAMP signaling
GLP-1
IBMX
epinephrine
SST
pramlinitide
C
Calcineurin signaling
tacrolimus
cyclosporin A
okadaic acid
D
Endonucleases
APY29
sunitinib
E
ER pumps & channels
ryanodine
xestospongin
thapsigargin
F
Insulin signaling
staurosporine
AICAR
AS1842856
wortmannin
metformin
HNMPA
LY294002
S961
G
Nuclear receptors
rosiglitazone
dexamethasone
H
Nutrients
sodium butyrate
arginine
palmitic acid
I
Excitability
tolbutamide
diazoxide
verapamil
J
Protein degradation
tunicamycin
MG132
eeyarestatin I
bortezomib
K
Transcription
triptolide
alpha amanitin
DRB
trichostatin A
MGCD0103
actinomycin D
L
Translation factors
cycloheximide
PKR inhibitor
PERK inhibitor I
DHBDC
CCT020312
isrib
sal003
azoramide
Relative GFP fluorescence intensity
Time (hours)
M
GFP fluorescence
Cell death
GLP1
IBMX
staurosporine
sodium butyrate
arginine
palmitic acid
rosiglitazone
PKR inhibitor
azoramide
thapsigargin
AICAR
ETOH
epinephrine
tunicamycin
DHDBC
verapamil
bortezomib
DMSO
wortmannin
S961
tolbutamide
PERKi I
ISRIB
sal003
SST
metformin
cyclosporin A
xestospongin
MG132
ryanodine
trichostatin A
HNMPA
tacrolimus
okadaic acid
diazoxide
dexamethasone
APY 29
triptolide
alpha amanitin
DRB
cyclohexamide
LY294002
MGCD0103
AS1842856
pramlinitide
CCT020312
sunitinib
actinomycin D
eeyarestatin I
Treatment category
control
calcineurin
cAMP signalling
endonucleases
ER channels
insulin / other signalling
nuclear receptors
nutrients
plasma membrane excitability
protein degradation
transcription
translation factors
-log10 (p-value)
0
1
2
3

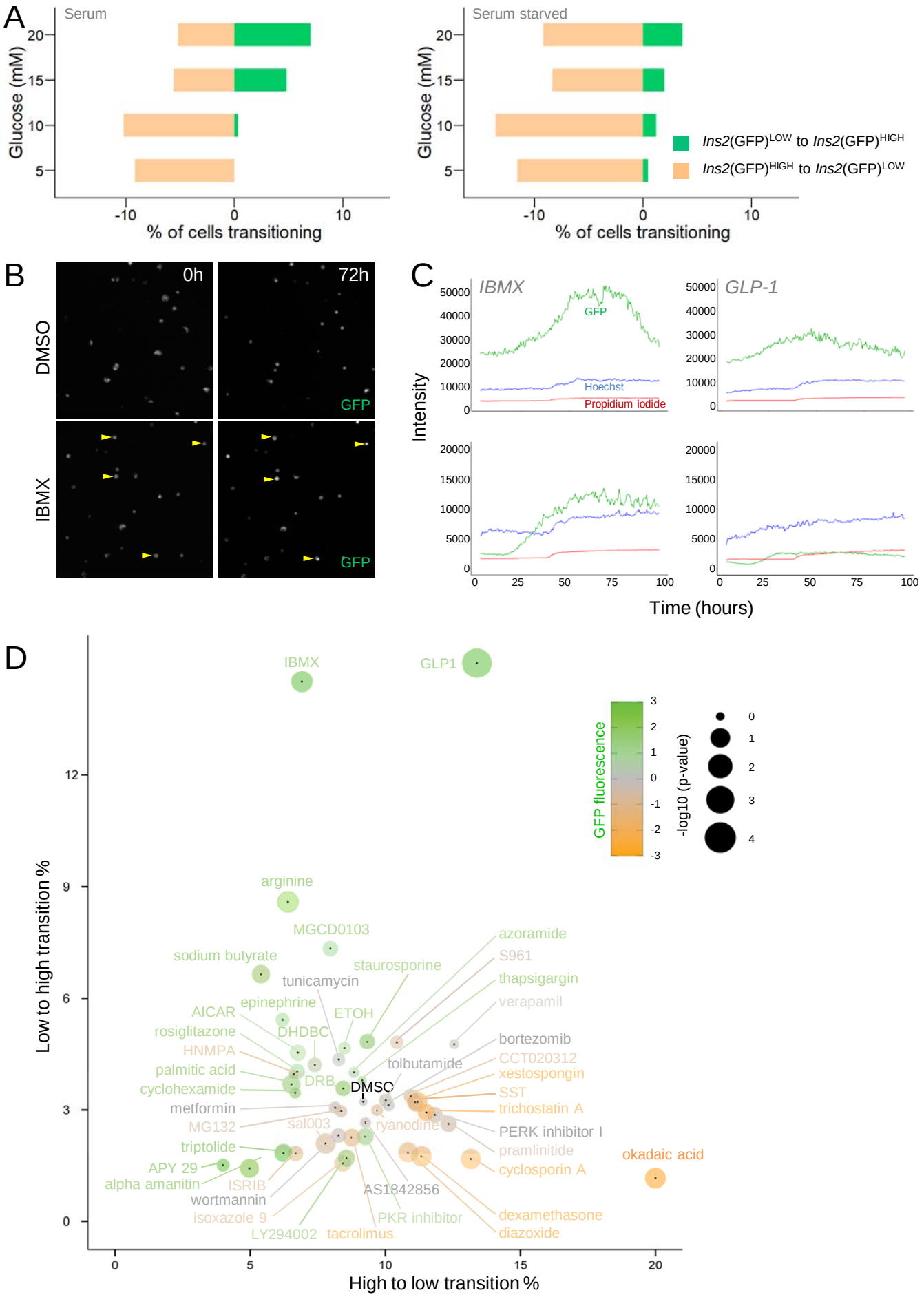
A
Serum
Serum starved
Glucose (mM)
% of cells transitioning
Ins2(GFP)LOW to Ins2(GFP)HIGH
Ins2(GFP)HIGH to Ins2(GFP)LOW
B
0h
72h
DMSO
IBMX
GFP
C
IBMX
GLP-1
Intensity
Hoechst
Propidium iodide
Time (hours)
D
IBMX
GLP1
GFP fluorescence
-log10 (p-value)
Low to high transition %
High to low transition %
arginine
MGCD0103
sodium butyrate
tunicamycin
staurosporine
azoramide
S961
thapsigargin
verapamil
epinephrine
AICAR
ETOH
rosiglitazone
DHDBC
HNMPA
bortezomib
CCT020312
palmitic acid
tolbutamide
xestospongin
DRB
cyclohexamide
DMSO
SST
metformin
trichostatin A
MG132
sal003
ryanodine
PERK inhibitor I
triptolide
pramlinitide
okadaic acid
APY 29
cyclosporin A
alpha amanitin
ISRIB
AS1842856
wortmannin
isoxazole 9
PKR inhibitor
dexamethasone
LY294002
tacrolimus
diazoxide

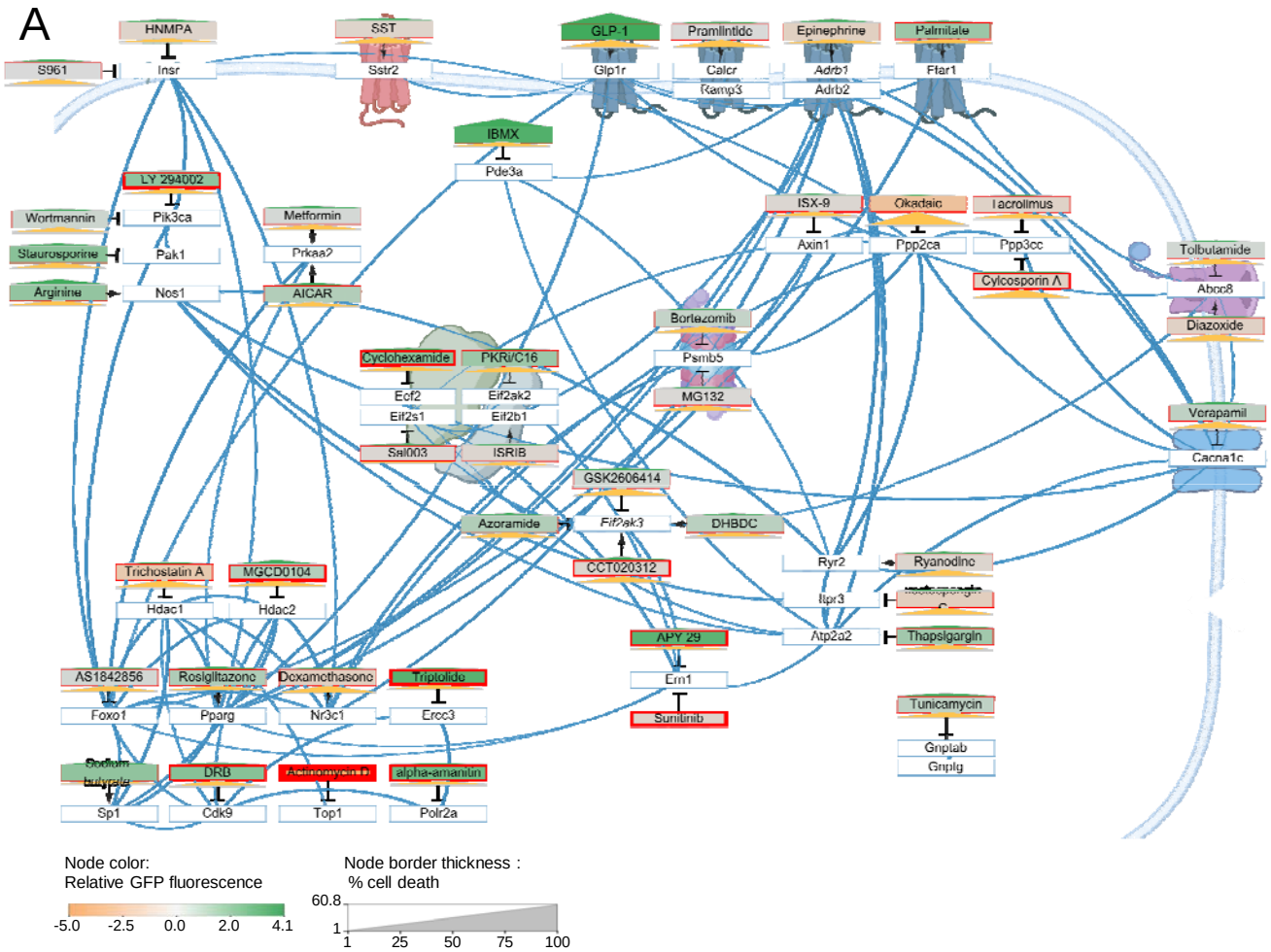
A
HNMPA
SST
GLP-1
Pramlintide
Epinephrine
Palmitate
S961
Insr
Sstr2
Glp1r
Calcr
Ramp3
Adrb1
Adrb2
Ffar1
IBMX
Pde3a
LY 294002
Wortmannin
Pik3ca
Staurosporine
Pak1
Arginine
Nos1
Metformin
Prkaa2
AICAR
ISX-9
Okadaic
Tacrolimus
Axin1
Ppp2ca
Ppp3cc
Cyclosporin A
Tolbutamide
Abcc8
Diazoxide
Bortezomib
Psmb5
MG132
Cyclohexamide
PKR/C16
Eif2
Eif2ak2
Eif2s1
Eif2b1
Sal003
ISRIB
Verapamil
Cacna1c
GSK2606414
Azoramide
Eif2ak3
DHBDC
CCT020312
Ryr2
Ryanodine
Itpr3
Atp2a2
Thapsigargin
Trichostatin A
MGCD0104
Hdac1
Hdac2
APY 29
Ern1
Sunitinib
AS1842856
Rosiglitazone
Dexamethasone
Triptolide
Foxo1
Pparg
Nr3c1
Ercc3
Tunicamycin
Gnptab
Gnplg
Sodium butyrate
DRB
Actinomycin D
alpha-amanitin
Sp1
Cdk9
Top1
Polr2a
Node color:
Relative GFP fluorescence
-5.0
-2.5
0.0
2.0
4.1
Node border thickness :
% cell death
60.8
1
1
25
50
75
100